

Inversion of extensional basins parallel and oblique to their boundaries: Inferences from analogue models and field observations from the Dolomites Indenter, eastern Southern Alps

Anna-Katharina Sieberer¹, Ernst Willingshofer², Thomas Klotz¹, Hugo Ortner¹, Hannah Pomella¹

5 ¹Department of Geology, University of Innsbruck, Innsbruck, 6020, Austria

²Department of Earth Sciences, Utrecht University, Utrecht, 3584 CB, Netherlands

Correspondence to: Anna-Katharina Sieberer (anna-katharina.sieberer@uibk.ac.at)

Abstract. Polyphase deformation of continental crust is analysed through physical analogue models for settings where platform-basin geometries at passive continental margins are subject to subsequent shortening and orogenesis. In a first stage,

10 segmentation of the brittle and brittle-ductile models into basins and platforms is achieved by extension. Basins are partly filled with brittle material to allow for a strength difference between basin and platform realms, simulating relatively weaker, incompetent deposits of grabens surrounded by competent pre-rift basement or carbonate platform rock, respectively. In a second stage of deformation, contraction parallel and oblique (10 to 20 degrees) to the basin axes has been applied leading to the inversion of earlier formed basins. The experiments show that strength contrasts across platform-basin transitions controls

15 the localisation and overall style of compressional deformation, irrespective of the nature of the basal décollement (frictional versus viscous), the rheology of the basin fill, or changing platform-basin thickness ratios. Orientations of thrust faults change laterally across inherited platform-basin transitions throughout all experiments; higher obliquity of basin inversion leads to stronger alignment of thrust curvature to the orientation of pre-existing rift axes. At individual thrust faults, variations in the strike of thrust fronts are accompanied with changes of the shortening direction during incremental phases of deformation.

20 Reactivation of normal faults occurs in oblique basin inversion settings only, favourably at platform-basin transitions where the normal faults face the shortening direction. The amount and style of fault reactivation depend on the material used. Our experiments are relevant for natural cases such as the Dolomites Indenter of the eastern Southern Alps underlining the importance of inherited geologic features for the subsequent shortening geometries. Field structural data from the western segment of the Belluno thrust of the Valsugana fault system support predicted variations of thrust fault orientation and a lateral

25 change in shortening direction (from SSW to SSE along strike) along one single fault. Based on our modelling results, we suggest that this variability of thrust fault orientation and shortening directions, controlled by inherited structures, is consistent with strain partitioning during a single phase of deformation and does not necessarily reflect different deformation phases.

Keywords. Crustal-scale analogue modelling, parallel to oblique basin inversion, polyphase deformation, lateral strength contrasts, eastern Southern Alps, Dolomites Indenter.

1 Introduction

Shortening of passive continental margins is often associated with the reactivation of inherited normal faults, inversion of sedimentary basins, and their incorporation in fold- and thrust belts (e.g., Turner and Williams, 2004; Cooper and Warren, 2020). Inverted sedimentary basins are known from numerous orogenic settings worldwide, from, e.g., the European Alps

35 (Boutoux et al., 2014; Gillcrist et al., 2015; Granado et al., 2016; Oswald et al., 2018; Héja et al., 2022), the Apennines (Scisciani et al., 2001; Pace et al., 2014), the Pyrenees (Tavani et al., 2011; Mencos et al., 2015), Iberia (Ramos et al., 2017), the Atlas Mountains of Morocco (Beauchamp et al., 1999) and Algeria (Bracène and Froizon De Lamotte, 2002), and from the South American Andes (Kley and Monaldi, 2002; Giambiagi et al., 2003; Kley et al., 2005; Carrera et al., 2006). Analogue modelling is frequently used for studying complex and large-scale 3D deformation patterns resulting from superposed

40 extensional and compressional deformation phases (e.g., Buchanan and Mcclay, 1991; Sassi et al., 1993; Brun and Nalpas, 1996; Amiliba et al., 2005; Panien et al., 2005; Mattioni et al., 2007; Yagupsky et al., 2008; Cerca et al., 2010; Yamada and Mcclay, 2010; Bonini et al., 2012; Di Domenica et al., 2014; Granado et al., 2017; Deng et al., 2020; Zwaan et al., 2022). Together with numerical modelling (Buiter et al., 2006; Panien et al., 2006; Buiter et al., 2009; Granado and Ruh, 2019; Ruh, 2019) fundamental insights are obtained allowing to infer favourable mechanic and kinematic conditions for basin inversion.

45 These studies confirm conceptual ideas (e.g., Sibson, 1985) and demonstrate that fault reactivation in inversion settings indeed strongly depends on the orientation and the dip angle of pre-existing faults or crustal discontinuities and on the rheology of rocks in foot- and hanging walls. Additionally, a combination of lateral, stratigraphically controlled, mechanical variations and pre-existing structures in basement or cover sequences often controls the location of transfer zones, which connect different styles of deformation along strike of thrust belts (Thomas, 1990).

50 Within the European Alps, a prominent example of inverted sedimentary basins, which are now part of a fold- and thrust belt, is the eastern Southern Alps. The relationship between Mesozoic extension, resulting in laterally distinct stratigraphic successions related to the structuration of the Adriatic crust into basins and platforms (Bernoulli and Jenkyns, 1974; Winterer and Bosellini, 1981; Sarti et al., 1992; Bertotti et al., 1993), and Cenozoic compression was intensively discussed by Doglioni (1987, 1991, 1992), as their interaction is crucial to understand the tectonic evolution of the eastern Southern Alps. Based on

55 field evidences from the Dolomites (eastern Southern Alps east of Bozen/Bolzano, west of the Cadore region and N of Valsugana fault system) and the Venetian Pre-Alps (eastern Southern Alps south of Valsugana fault system towards the Venetian plain) (Doglioni, 1991, 1992; Schönborn, 1999), and from the Friuli-Alps (eastern Southern Alps east of Cadore region, W of the Italian-Slovenian border) (Nussbaum, 2000), contrasting ideas for the evolution of inversion structures were proposed.

60 Through a series of crustal scale analogue experiments, we investigate the effect of an early extensional phase leading to differentiation of the crust in platforms and basins on a later compressional phase, which is relevant for the discussion of inversion tectonics in settings such as the eastern Southern Alps. In particular, we test the hypothesis that pre-existing NNE-SSW trending normal faults are of paramount importance for understanding and explaining Paleogene to Neogene crustal

deformation of the Dolomites Indenter. More precisely, we aim at demonstrating causal relationships between lateral changes
65 of thrust fault orientations and the inherited fault-bound basin to platform transitions in extended crust. We substantiate our
findings by comparison with field observations, e.g., with the Belluno area, where the western (i.e., Trento) platform merges
into the eastern (i.e., Belluno) basin.

2 Geological setting of the Dolomites Indenter

In continent-continent collision settings, an indenter is defined as a piece of relatively rigid continental lithosphere which,
70 upon collision, deforms weaker lithosphere in front (Tappognier et al., 1986). In the evolution of the European Alps, the
Adriatic plate is traditionally considered as rigid tectonic element often referred to as Adriatic Indenter (e.g., Schmid et al.,
2004) and research mainly focused along its confining fault system, e.g., the Periadriatic fault system, the Giudicarie belt, and
75 the Valsugana and Montello fault systems (Fig. 1) and areas to the north elucidating collision and extrusion tectonics
(Ratschbacher et al., 1991; Scharf et al., 2013; Favaro et al., 2017; Rosenberg et al., 2018). Following Schmid et al. (2004),
we use the term Adriatic (micro)plate as part of greater Apulia which is located south of the Periadriatic fault system; Apulia
being paleogeographically understood as consisting of all continental realms between the Neotethys in the south and the Alpine
Tethys in the north. However, the structure of the northernmost part of the Adriatic microplate within the eastern Southern
80 Alps of Italy and Slovenia, referred to as Dolomites Indenter (Rosenberg et al., 2007), demonstrates significant internal
deformation. This continental indenter contains the structural memory of Permian and Late Triassic to Early Jurassic
extensional phases, which possibly controls thrust fault orientations related to Neogene to recent fold-and-thrust belt formation
(Bosellini, 1965; Doglioni, 1992) in the eastern Southern Alps, with mainly in-sequence deformation towards its external
southern parts (Sell, 1998; Castellarin et al., 2006).

The eastern Southern Alps are bordered by the Pustertal-Gailtal fault (a part of the Periadriatic fault system) to the north, the
Venetian plain to the south and the Giudicarie fault system and the Giudicarie belt to the west (Fig. 1a). The term “eastern
85 Southern Alps” is used synonymously to “Dolomites Indenter” and refers to the eastern part of the Adriatic Indenter. Therefore,
the Dolomites Indenter represents the front of the Neogene to ongoing N(W)-directed continental indentation of Adria into
Europe. The indentation leads to the offset of the Periadriatic fault system along the Giudicarie fault system (Pomella et al.,
2011), to the doming of the Tauern Window (Scharf et al., 2013; Schmid et al., 2013; Favaro et al., 2017; Rosenberg et al.,
2018), to eastward lateral extrusion of crustal fragments of the Eastern Alps (Ratschbacher et al., 1991; Rosenberg et al., 2007),
90 and to overall S-directed folding and thrusting of the eastern Southern Alps (Doglioni and Bosellini, 1987). In the following
sections we characterise the Permian to Jurassic extension and Paleogene to Neogene shortening of the Dolomites Indenter in
order to assess whether and how inherited platform-basin geometries affect younger, Alpine deformation.

[Figure 1]

95 **2.1 Permian to Jurassic extensional phases**

A first rifting event affecting the Adriatic crust started during the Early Permian and was related to large-scale intracontinental dextral transform shear (Muttoni et al., 2003) (or to the opening of the Neotethys (i.e., Meliata-Hallstatt Ocean) according to, e.g., Stampfli and Borel, 2002; Stampfli et al., 2002; Schmid et al., 2004). Late Permian to Upper Triassic (Carnian) extension (Bertotti et al., 1993) lead to the formation of N-S striking normal faults and ENE striking transfer faults (Doglioni, 1991), 100 accompanied by the deposition of the up to ~2 km thick Athesian Volcanic Complex (Bosellini et al., 2007; Morelli et al., 2007; Marocchi et al., 2008; Brandner et al., 2016) (Figs. 1b, 2a). A second rifting event during the Late Triassic to Early Jurassic, associated with the opening of the Alpine Tethys (Sarti et al., 1992; Schönborn, 1999; Nussbaum, 2000; Masetti et al., 2012; Picotti and Cobianchi, 2017) (or to the opening of the Neotethys Ocean according to, e.g., Vrabec et al., 2009), 105 segmented the Adriatic passive continental margin into submarine carbonate platforms and basins, which are bordered by N(NE)-S(SW) striking, crustal-scale normal faults (Winterer and Bosellini, 1981; Doglioni, 1991; Sarti et al., 1992; Bertotti et al., 1993; Selli, 1998; Busetti et al., 2010; Picotti and Cobianchi, 2017; Le Breton et al., 2021) (Figs. 1b, 2b). These normal faults reach into the middle crust to depths of about 10 to 20 km (e.g., Pogallo fault in Handy, 1987; Lugano fault in Bertotti, 1990), and are associated with minor normal faults reaching down to about 4 to 7 km depth (Bertotti et al., 1993).

From west to east, four major domains, bounded by N-S striking rift faults, were formed: the Lombardian basin, the Trento 110 platform, the Belluno basin, and the Friuli platform (Winterer and Bosellini, 1981) (Figs. 1b, 2). The Lombardian basin has the Ballino-Garda line, which is part of the Giudicarie belt, at its eastern border towards the Trento platform and therefore belongs to the western Southern Alps. The Trento platform is located east of the Ballino-Garda line and is split into a northern and a southern part by the SW-NE trending Valsugana fault system. The northern Trento platform shows differential syn-sedimentary subsidence (Sarti et al., 1992; Martinelli et al., 2017) (Figs. 1b, 2) and its location approximately coincides with 115 the extent of the Permian Athesian Volcanic Complex (Fig. 1b). The southern Trento platform (i.e., Venetian Pre-Alps) shows a thicker and more continuous sedimentary cover than the northern Trento platform (Fig. 2a). The Belluno basin is narrower and shows a more complex geometry compared to basins west of the Ballino-Garda line as it is N-trending in its central part, but NE-trending towards the Carnia region (Sarti et al., 1992). Whether and how the Belluno basin merges into the Slovenian basin, located north of the Friuli platform and NE of the Belluno basin (Fig. 1b), is topic of discussions (Smuc and Goričan, 120 2005; Van Gelder et al., 2015). The Friuli platform (i.e., Dinaric carbonate platform in Smuc, 2005) shows stable shallow water sedimentation during most of the Jurassic and Cretaceous (Nussbaum, 2000; Merlini et al., 2002; Kastelic et al., 2008; Picotti and Cobianchi, 2017; Moulin and Benedetti, 2018) and transitions to the vast Adriatic carbonate platform (Vlahović et al., 2005) to the southeast.

125

[Figure 2]

2.2 Paleogene to Neogene shortening

Continental collision between Adria and Europe resulted in a first compressional phase (i.e., Pre-Adamello phase) within the western Southern Alps (i.e., Insubric Indenter west of the Giudicarie belt; Rosenberg et al., 2007) which is mostly S-directed
130 (Schönborn, 1990; Carminati et al., 1997), preceding the Adamello intrusion and therefore pre-middle Eocene in age (Zanchi et al., 2012; Zanchetta et al., 2013) and not documented within the eastern Southern Alps (Castellarin et al., 1992). During the Paleogene, the eastern Southern Alps were in a foreland, pro-wedge position to Dinaric post-collisional shortening (Ustaszewski et al., 2010). Especially the eastern part of the eastern Southern Alps, from Gadertal/Val Badia eastward, shows mainly thin-skinned (Doglioni, 1987), WSW- to SW-directed Dinaric shortening (Doglioni and Bosellini, 1987; Caputo, 1996;
135 Keim and Stingl, 2000; Nussbaum, 2000) of about 10-15 km (Doglioni, 1992), whereas the western Venetian plain and the western Dolomites were representing the foreland to the external Dinarides (Poli et al., 2021). After a short phase of extension and transtension accompanied by volcanism (i.e., Veneto Volcanic Province, Zampieri, 1995; Beccaluva et al., 2007) within the southern Trento platform, NE of Verona (Fig. 1b), SSW-directed shortening in the eastern Southern Alps starts in Late Oligocene and SSE-directed shortening in Miocene (Venzo, 1940; Castellarin et al., 1992; Castellarin and Cantelli, 2000)
140 times. From the Late Oligocene onwards, the eastern Southern Alps represent the retro-wedge of the Alpine orogen (Castellarin and Cantelli, 2000). The Late Triassic to Jurassic platform-basin configuration was shortened and inverted; the Dinaric fold-and-thrust belt got overprinted by overall SSE-directed deformation (Mellere et al., 2000; Placer et al., 2010). From north to south, the major Neogene faults within the eastern Southern Alps are (i) the Valsugana fault system, including Valsugana and Belluno thrusts and its N-directed back-thrusts, the Villnöss/Funes and Würzjoch/Passo delle Erbe faults (ii) the blind Bassano-
145 Valdobiadene thrust with the Bassano anticline in its hanging wall and its N-directed back-thrust, the Val di Sella back-thrust (Sell, 1998), and (iii) the blind Montello thrust with the Montello anticline in its hanging wall, representing the most external structural feature of the eastern Southern Alps (Picotti et al., 2022).

The main shortening phase within the Dolomites Indenter (i.e., Valsugana phase) takes place during the Miocene (17-9 Ma), and is constrained by scarce thermochronological data (Zattin et al., 2006; Pomella et al., 2012; Heberer et al., 2017).

150 Crystalline basement in the hanging wall of the Valsugana thrust clearly shows Neogene thick-skinned thrusting in the western part of the eastern Southern Alps (i.e., western Dolomites), but does not crop out in eastern part of the eastern Southern Alps (Friuli region) above the main thrust. Serravallian to Tortonian sediments are deformed by the Valsugana thrust (Doglioni, 1992), representing the final push along the Valsugana fault system. Further south, Pliocene sediments are folded above the frontal triangle zone of the Montello thrust (Venzo, 1977). According to recent studies of Anderlini et al. (2020), Joz
155 Najafabadi et al. (2021), and Picotti et al. (2022), the Bassano-Valdobiadene and the frontal Montello thrusts are seismically active at present.

Mesozoic structures are frequently reactivated during the Neogene, as, e.g., the Permian normal Calisio and Schio-Vicenza faults as strike-slip faults or cross-cut in shallower angles as, e.g., the dextral Paleo-Valsugana fault (Sell, 1998). Normal faults related to platform-basin transitions are reactivated according to their dip angle and dip direction and lead to lateral

160 ramps for Neogene thrusts. According to Doglioni (1992), E-dipping Mesozoic normal faults have predominantly been cut and involved in the Alpine fold-and-thrust belt without major reactivations, whereas W-dipping Mesozoic normal faults seem often to be strongly deformed and reused as thrust planes or by sinistral transpression, as it is the case for, e.g., the Giudicarie belt. In the eastward prolongation of the Bassano-Valdobiadene thrust, at the transition of Belluno basin and Friuli platform, the Caneva line (i.e., Cansiglio line) represents a lateral ramp (Doglioni, 1991; Schönborn, 1999; Picotti et al., 2022). Neogene
165 structures stack platform regions onto basin regions, as, e.g., the Belluno thrust, which brings competent successions of the Trento platform onto more incompetent stratigraphy of the Belluno basin (Doglioni, 1991, 1992).

The amount of shortening along the Valsugana fault system is approximately 15 km (Sell, 1998). However, recent studies show 6 to 8 km of shortening along the Belluno fault only (Zuccari et al., 2021), leading potentially to more shortening along the whole Valsugana fault system. According to Verwater et al. (2021), the amount of shortening across the eastern Southern
170 Alps depends on competence contrasts and on thickness variations of sedimentary successions due to laterally heterogeneous paleogeographic domains. Therefore, competent platform successions show less shortening compared to basinal regions as, e.g., the Belluno basin, where the spacing of thrusts is especially narrow and the southern thrust front is located remarkable far north (Doglioni, 1992).

2.3 Sedimentary succession and mechanical significance

175 In general, the stratigraphy of the eastern Southern Alps is characterised by a Variscan metamorphic basement, Permian volcanic rocks (Athesian Volcanic Complex, limited to the northern Trento platform), and a Late Permian to Neogene sedimentary succession (Winterer and Bosellini, 1981) (Fig. 2). The sedimentary succession shows minor differences in W-E extent across Adria during the Late Permian and Triassic, except stronger subsidence in the Lombardian basin (Sarti et al., 1992; Bertotti et al., 1993; Picotti et al., 1995) and stronger Ladinian volcanism in the western part of the eastern Southern
180 Alps, but becomes strongly heterogeneous during Late Triassic to Jurassic extension (syn-rift sediments). Lateral and vertical facies changes known from several places within the eastern Southern Alps are expressions of the platform-basin configuration of the Mesozoic passive continental margin (Abbots, 1989; Doglioni, 1992; Picotti and Cobianchi, 1996; Sell, 1998; Franceschi et al., 2014; Picotti and Cobianchi, 2017).

Especially the northern Trento platform shows remarkable unconformities from the Jurassic onwards with, e.g., a fully eroded
185 Mesozoic cover on top of the Athesian Volcanic Complex or a strongly reduced Jurassic (Winterer and Bosellini, 1981; Beccaro et al., 2002) to Cretaceous (Lukeneder, 2010) succession overlying the Athesian Volcanic Complex north of the Valsugana fault system (Fig. 2a). Within the southern Trento platform, the stratigraphic succession reaches into the Paleogene to Miocene (Fig. 2a) with limestone and marls (Doglioni and Carminati, 2008; Vignaroli et al., 2020). During the lower Jurassic, at the footwall of the major normal faults of the Trento and Friuli platforms, massive shallow water carbonates were
190 deposited, whereas deep-water sediments occurred in the Belluno basin; oolitic limestone, shed from the platforms, transitions both realms (Masetti et al., 2012; Franceschi et al., 2014; Masetti et al., 2017; Picotti and Cobianchi, 2017) (Fig. 2b). The

Slovenian basin shows a sediment thickness comparable to the Belluno basin (Fig. 2), but developed earlier (Ladinian) and is deeper marine (Goričan et al., 2012; Rožič et al., 2018).

The main detachment horizon for thick-skinned deformation in the eastern Southern Alps is located at depth between 15 and 195 20 km, supported by recent local earthquake data (Jozi Najafabadi et al., 2021). For thin-skinned deformation, the two main detachment horizon are (i) evaporite-bearing shales of the Late Permian to Early Triassic Bellerophon Formation (Doglioni and Bosellini, 1987; Nussbaum, 2000), which thickens from W (no Bellerophon Formation west of Val d'Adige/Etschtal) to E, reaching a maximum thickness of approximately 400 m in the E (Noé, 1987; Massari and Neri, 1997), and therefore the main detachment for SW-directed Dinaric structures and (ii) the alternate succession of evaporite, shales, and marls of the 200 Carnian Raibl Group (Nussbaum, 2000) with a maximum thickness of about 250 m (De Zanche et al., 2000).

3 Analogue modelling approach

Inspired by the case of the Dolomites Indenter (section 2), a series of 12 crustal-scale brittle and brittle-ductile analogue experiments provide insights in the structural evolution of continental upper to middle crust subject to extension followed by contraction. The experiments are designed such to allow for the opening of multiple extensional basins separated by platform-205 type areas, a structural configuration that is frequently observed in passive margin settings where the continental shelf is dissected by graben structures and where the shelf transitions to deep basins (Mandl, 2000; Berra et al., 2009; Sapin et al., 2021). Contraction of earlier formed graben structures of variable width allows for testing the influence of inherited structures 210 and basin geometries on the style of a younger contractional deformation phase, as well as timing and localisation of uplift of the inverted graben structures and their transition to platform areas. Key parameters of this study include (i) the angle of obliquity (0°, 10° or 20°) of shortening with respect to the strike of the first phase rift structures, (ii) the basal décollement rheology, and (iii) the basin fill rheology, and form the basis for grouping the experiments in three major sets (Table 1). The experiments have been designed to allow comparison with the Dolomites Indenter of the eastern Southern Alps, but are also relevant for other regions where rift structures are inverted at low angle to the rift axes.

215

[Table 1]

3.1 Set-up and geometries of analogue models

Model setups and the modelling results are described within a geographic frame where the north direction is aligned with the 220 strike of the velocity discontinuities (VD1 and VD2) and thus the strike of the basin axes (Fig. 3a-c). All experiments are built on a table and on top of one fixed and two mobile plastic sheets of 1 mm thickness. Positioning the VDs obliquely with respect to the backstop allows for the formation of graben structures at angles of 10 and 20 degrees to the shortening direction (Fig. 3a-c). The mobile plastic sheets are attached to two individual engines which simulate extension by pulling the mobile sheets

in opposite directions from underneath the fixed sheet at constant velocity of 5 cm/h or 2.5 cm/h for brittle or brittle-ductile experiments, respectively (Table 1, Fig. 3a-c). Lower velocities yield differential stresses for the ductile layers, that allow for 225 mechanical decoupling at the transition from brittle to ductile layers, ensuring that the ductile layer acts as a décollement. As such the transition from the fixed to the mobile plastic sheets predefines VDs along the western and eastern margins of the fixed plastic sheet. This kinematic boundary condition leads to asymmetric extension on either side of the fixed sheet comparable to proposed extensional geometries of the northern Adriatic plate margin (Sarti et al., 1992; Masetti et al., 2012). The extensional phase was terminated after 5 cm of displacement of the eastern mobile sheet, whereas it continued to 9 cm of 230 displacement at the western mobile sheet (Fig. 3a-c), leading to sedimentary basins of different size comparable to the relatively narrow Belluno and wide Lombardian basins in the Southern Alps (Winterer and Bosellini, 1981; Bertotti et al., 1993; Picotti and Cobianchi, 2017).

[Figure 3]

235

Additional to pre-existing discontinuities and obliquity in basin inversion we apply lateral strength contrasts resulting from (i) pre-existing deformation due to the extensional phase, (ii) syn-extensional basin fill material, and (iii) lower thickness of the 240 basinal succession compared to the platform succession. Using different material for the basin fill than for platforms simulates relatively weaker, incompetent graben deposits compared to surrounding competent pre-rift basement or carbonate platform rock, respectively. In our analogue models we tackle this by using, e.g., homogeneous layers of quartz sand for the initial, non-stretched model, simulating competent crust, which was extended in a first phase of deformation. Syn- to post-extensional sedimentation has been applied in the resulting grabens by manually sieving either quartz sand, feldspar sand or glass beads 245 into the graben structures after approximately each cm of extension (Fig. 4a). The resulting grabens were filled up to a platform-basin thickness ratio of (i) 0.7 to 0.8 for underfilled basins using quartz sand only (models 1-7) or (ii) 1 for filled basins using either quartz sand (model 8), feldspar sand (model 9), or glass beads (models 10-12), simulating relatively incompetent rock compared to the platforms (Fig. 4a). Minor thickness variation of underfilled basins (models 1-7) is a consequence of the handling technique. For platform-basin ratios of 1, lateral strength differences between platforms and basins are achieved by varying the material properties of the basin fill.

Once the extensional phase is finished, the mobile plastic sheets are detached from their engines and fixed to the table.

250

Subsequent contraction of the extensional basins is achieved by pushing the rigid backstop at constant velocity into the experiment. The velocity of the moving wall is 3 cm/h or 2.5 cm/h for brittle or brittle-ductile experiments, respectively (Table 1). The compressional phase was terminated after 9 cm of shortening. Experiments consisting of brittle material only are confined by a rigid backstop in the north, aluminum bars in the east and west and have an open boundary in the south, whereas 255 brittle-ductile models also have their southern boundary confined with aluminium bars to prevent the outflow of ductile material. Most other oblique inversion models show a kink in the transition from the western basin to the western platform, because of limited space of setup arrangements. This simplification does not influence the modelling results, because

shortening is stopped prior to deformation reaching this kink. However, a wider backstop was used in experiments 7 and 8 to test the sensitivity of modelling results on model size. An overview of modelling setups is provided in Table 1.

260

[Figure 4]

3.2 Model material and scaling

The analogue experiments presented in this study consist of brittle or a combination of brittle-ductile layers representing continental upper crust, which is either entirely brittle or brittle with a ductile layer at the base (Fig. 4a). The latter simulates 265 crustal layers below the brittle-ductile transition (models 6 and 7). Layers of colored, dry quartz sand represent the brittle pre- rift crust in all models, whereas the ductile layer consists of polydimethylsiloxane (PDMS silicon polymer), mixed with Rhodorsil gomme, representing the ductile crust below the brittle-ductile transition. The ductile material has a density of 1500 kg/m³, a viscosity of 3.8×10^4 Pas, and shows slightly non-Newtonian behaviour ($n = 1.15$) (Table 2). The properties of the 270 ductile material have been determined with a pycnometer and a coni-cylindrical viscometer, respectively. Variations to these setups entail a layer of glass beads at the base of the brittle crust simulating a weak, frictional décollement comparable to what 275 has been used by Cotton and Koyi (2000). The influence of sediment strength on subsequent deformation geometries during the inversion phase is accounted for by varying the granular material representing the syn-extensional sediments. These include quartz sand (model 8), feldspar sand (model 9) and glass microbeads (models 10-12). The mechanical properties of all brittle and ductile materials used in this study are summarized in Table 2 and are described in detail in Klinkmüller et al. (2016) and Willingshofer et al. (2018).

[Table 2]

Scaling of all models follows scaling procedures described in the pioneering works of Hubbert (1937) and Weijermaars and 280 Schmeling (1987). With a length-scale ratio of L^* ($L_{\text{model}}/L_{\text{nature}}$) = 1.25×10^{-6} , 1 cm in the model represents 8 km in nature (1:800.000). As such the initial and final model widths (after extension) scale to 352 and 464 km in nature, respectively. For 285 modelling contraction of oblique rift structures, models 7 and 8 have been increased in width to minimize boundary effects; a larger backstop leading to a final model width of 73 cm, scaling to 584 km in nature, was used. For the adopted length scaling, the brittle-ductile transition of our analogue models is at a depth of 16 km in nature, which agrees with earlier published estimates of the brittle-ductile transition in the eastern Southern Alps (Willingshofer and Cloetingh, 2003; Viganò and Martin, 2007; Laubscher, 2010). At this depth the vertical stress (i.e., lithostatic stress) in, e.g., the platform regions of our experiments, is 590 Pa, corresponding to 880 MPa in nature, which results in a stress-scale ratio of 6.7×10^{-7} . Strength profiles (Fig. 4b) are representative for the initial conditions and have been calculated following Weijermars (1997); Brun (2002). The density-scale 290 ratio ρ^* ($\rho_{\text{model}}/\rho_{\text{nature}}$) yields 0.54 as the density of our model material, e.g., quartz sand, is 1500 kg/m³, representing densities

290 of 2800 kg/m^3 of natural upper to middle crust (e.g., Ebbing, 2004; Faccenda et al., 2007; Šumanovac et al., 2009). The velocity for our brittle-ductile models is scaled after a time-scale ratio $t^* = 1.93 \times 10^{-11}$ calculated as:

$$t^* = \frac{1}{\varepsilon^*} \quad (1)$$

with ε^* referring to the shear strain rate ratio equaling:

$$\varepsilon^* = \frac{v^*}{L^*} \quad (2)$$

295 where the velocity ratio v^* is 6.49×10^4 and scales 2.5 cm/h of model velocity rate to 0.33 cm/a to nature, representing 50 km of shortening within a period of 15 Ma . This shortening rate correlates well with estimates from orogenic belts such as the eastern Southern Alps (Doglioni, 1987, 1991; Nussbaum, 2000). The velocity of the moving wall for brittle-ductile experiments simulates a compressional model strain rate of 1.13×10^{-3} , corresponding to 2.18×10^{-14} in nature. The viscosity of the ductile model material of $3.8 \times 10^4 \text{ Pas}$ scales to natural viscosities of approximately 10^{21} Pas , representing quartz dominated ductile 300 middle crust below the brittle-ductile transition (Hirth et al., 2001).

3.3 Monitoring and analysis of experiments

During the experimental runs, the model surface is monitored by top-view photographs (using a Panasonic Lumix DC-G9 with 20.3 megapixels) and a 3D surface scanner in order to trace changes in surface deformation. Top-view pictures and 3D surface scans have been taken at regular time intervals. For brittle and brittle-ductile experiments, the translation displacement between 305 two successive top-view photographs is 0.15 cm and 0.125 cm , between two surface scans 0.75 cm and 0.625 cm , respectively. Adding coffee grains as tracers on the model surfaces facilitated calculating incremental particle displacements using particle image velocimetry (PIV) analysis (PIVlab, Thielicke and Stamhuis, 2004) and PIV-derived strain analysis (strainmap, Broerse et al., 2021). The strainmap tool of Broerse et al. (2021) further enables to determine strain types (e.g., extension, strike-slip, shortening and transitions) occurring during the respective model runs from the ratio of the largest to the smallest principal 310 strain. The conversion of 3D surface scan data into digital elevation models enables tracing of the topographic evolution during the compressional deformation phase. After the model run, layers of black and natural coloured quartz sand are implemented as post-kinematic covers in order to preserve topography. Water sprinkled on the sand increases cohesion and enables sectioning the experiments for studying internal deformation in 2D. Photographs of 2D cross-sections (using Panasonic Lumix DC-G9 with 20.3 megapixels) are then put back together to a quasi 3D model using Midland Valley's MOVE software, in 315 order to follow fault geometries laterally throughout the model.

3.4 Limitations and simplifications of analogue models

Potential influences leading to strain localisation like (i) surface processes (e.g., erosion or sediment transport), (ii) isostasy or (iii) temperature dependence of materials are absent in our physical analogue models. The viscosity of the ductile layer is therefore invariant to depth, what is widely accepted in analogue modelling studies (Davy and Cobbold, 1991), but can be 320 adapted through implementing appropriate uniform viscosities. The absence of an asthenospheric layer excludes isostatic

compensation of the model and therefore leads to an overestimation of the evolving topography. Shortening is mainly accommodated by (ductile) thickening close to the moving wall where strain localises to form symmetric fore- and back-thrusts. Despite those simplifications, the presented experiments resemble first-order deformation processes of a polyphase deformed continental crust and possible influences of erosion and sedimentation on the localisation of faults or on fault
325 geometries in general are acknowledged (Graveleau et al., 2012).

4 Modelling results

In the following sections, the results of our analogue modelling study are described, starting with a detailed description of the “reference model” (model 1, Fig. 5). Thereafter we comparatively describe the models based on interpreted top-view photographs, interpreted cross-sections of the final stage of the specific experiment, PIV analyses, and PIV-derived strain
330 analyses. Note that the transpressional deformation at the western side of the western basin of model 7 and model 8 is a result of the modelling setup with a wider backstop and not relevant for comparison with the natural prototype. The term thrust system (i.e., thrust sheet) is used in the following for a combination of fore-thrust and accompanying back-thrust(s).

4.1 Reference model, model 1

Model 1 (Fig. 5) consists only of brittle material (quartz sand for both, platforms and basin fill) and basin inversion is parallel
335 to the strike of the rift structures. The strength difference between platforms and basins is simulated by a variation in thickness of the sand layers (i.e., underfilled basins) (Table 1, Figs. 3a and 4a). Model 1 serves as reference model as it is the relatively simplest experiment of our study, representing the starting point for changes of various parameters (parametric study, section 4.2) and for the gradual addition of complexity in the subsequent models.

During extension, two asymmetric graben structures, separated by one platform, form, each with a major, high-angle normal
340 fault above the basal VDs (i.e., west and east of the western platform; see interpreted top-view photograph in Fig. 5a, cross-section c-c' in Fig. 5g). As the basal kinematic boundary condition is opposite for both graben structures, the major normal faults dip in opposite directions. Large offset (1.2 cm in cross-section c-c' in Fig. 5g) normal faulting on the stationary side of the evolving graben is coeval with the formation of a large number of small-offset normal faults on the mobile side. All normal faults evolve perpendicular to the extension direction, are parallel to each other, appear straight, and dip towards the center of
345 the main graben with an average dip angle of 63°. At the end of extension, model 1 consists of two basins and two platforms, which are perpendicular to the backstop (Fig. 5a, cross-section c-c' in Fig. 5g). The crust was thinner at the locations of the basins (1.4 cm average thickness) compared to the platforms (2 cm), leading to a platform-basin thickness ratio of 0.7 representing lateral mechanical strength differences (Fig. 4b, cross-section c-c' in Fig. 5g), which simulates overall weaker basin domains (e.g., equivalent to alternations of limestone, marl, clay) compared to non-stretched platform areas (e.g.,
350 basement rock, carbonate platforms). Note that the strike-slip fault north of the eastern platform (Fig. 5a-d) is a result of the modelling setup, which bears no major implication for the modelling result during contraction.

Early stages of basin inversion (Fig. 5b) already show curved thrust faults forming at platform-basin transitions (thrusts 1 of thrust sheet I in Fig. 5b), where the relatively weaker basins transition to the stronger platforms. The evolving thrust faults show anastomosing orientations at their fronts and cross-cut pre-existing normal faults without reactivation of the latter.

355

[Figure 5]

After 4.5 cm of shortening (Fig. 5c), a second, in-sequence thrust system II evolves, showing a curved thrust front, which is more distinct at the transition from the central western platform to the western basin than into the eastern basin. The cumulative strain map after 4.5 cm of shortening (Fig. 5d) shows shortening close to the backstop especially in and close to basinal areas (grey arrows in Fig. 5d), extension in the hanging wall of thrust system I within platform areas, and shortening at the fronts of both thrust systems I and II. Basin inversion is here most probably compensated by back-thrusting, as the orientation of early formed normal faults is not favourable for reactivation.

360 By the end of the contractional phase (Fig. 5e-f, cross-sections a-a' and b-b' in Fig. 5g), the thrust front of the third and most external thrust system III is located further towards the foreland on platforms than in basinal areas (Fig. 5e-f, cross-sections a-a' and b-b' in Fig. 5g). Deformation in basinal areas is represented by backstepping of oblique thrust fronts towards the hinterland (Fig. 5e-f, cross-sections a-a' and b-b' in Fig. 5g). Backstepping follows the orientation of the platform-basin boundary. In model 1, where platform-basin boundaries are parallel (0° obliquity) to the shortening direction, the orientation of the thrust front at the transition from platform to basin is at high angle ($\sim 55^\circ$) to the overall strike of the mountain belt.

365 370 Platform thrusts link with basin thrusts in the center of the respective basins (Fig. 5e-f).

Pre-existing normal faults are cross-cut by contractional faults and transported piggy back as shown in Fig. 5b-f. The extensional cumulative strain type which dominates the hanging walls of thrust systems I and II in platform areas (Fig. 5f), is a result of the passive uplift of thrust systems in the hinterland of the model orogen with in-sequence character. Passive uplift occurs along reactivated fore- and accompanying back-thrusts of the specific thrust systems. Fault reactivation is shown by 375 two separate back-thrusts (back-thrusts 4 and 5 in cross-section a-a' in Fig. 5g), which root in one single fore-thrust 3 (cross-section a-a' in Fig. 5g). Both back-thrusts 4 and 5 cross-cut fore-thrust 1 and therefore indicate a younger age. Reactivation of fore-thrust 3 leads to steepening of earlier formed thrusts and uplift of thrust system I (cross-section a-a' in Fig. 5g).

Overall, the style of thrusting documented in model 1 is a combination of foreland vergent pop-up systems, with in-sequence thrusting. Back-thrusts are either reactivated several times or formed new, meaning existing foreland-directed thrust faults 380 being cross-cut by younger back-thrusts (e.g., fore-thrust 1 being cut by back-thrusts 4 and 5 in cross-section a-a' in Fig. 5g).

The style of thrusting varies laterally, across platforms and basins, as both ramps and flats are longer on platforms (e.g., 4 cm ramp length of thrust 3 in cross-section a-a' in Fig. 5g) compared to those of basinal areas (e.g., 1.4 cm ramp length of thrusts 385 5 and 7 in cross-section b-b' in Fig. 5g), what is in accordance with the undulating surface expression of the thrust systems in map-view (Fig. 5e-f). The wavelengths of thrusts (i.e., the distance between the transition of lower flat to ramp of two adjacent thrusts) are longer on platforms compared to basin realms in parallel inversion models, e.g., 8.6 cm for platform hosted thrusts

3 to 6 (western platform, Fig. 5e-f, cross-section a-a' in Fig. 5g) and 6 cm for basin hosted thrusts 7 to 8 (eastern basin, Fig. 5e-f, cross-section b-b' in Fig. 5g). As normal faults are cut rather than reactivated during shortening, the basins are inverted and uplifted by closer spaced thrust imbrication compared to platforms (e.g., thrusts 4 and 7 in cross-section b-b' in Fig. 5g). This difference is related to thickness variations of the crust at the onset of shortening.

390 4.2 Parametric study

In the following, we describe and compare three sets of experiments, which focus on (i) the obliquity of inversion (Fig. 6), (ii) the basal décollement rheology (Fig. 8), (iii) the strength of the basin fill (Fig. 10), and compare the results to the reference model (model 1, Fig. 5).

4.2.1 Influence of obliquity of inversion

395 Models 2 (Fig. 6a-c) and 3 (Fig. 6d-f) represent models where the inversion has taken place at angles of 10 and 20 degrees with respect to the rift axes (Table 1, Fig. 3b-c), respectively. Similar to model 1, both models are brittle only, have a platform-basin thickness ratio of 0.7 to 0.8 (i.e., underfilled basin) (Table 1) and a syn-extensional basin fill consisting of quartz sand (Fig. 4a). Therefore, models 1-3 represent set 1 of our experiments and aim at studying the influence of obliquity (0, 10 and 20 degrees, respectively) of inversion on fault-reactivation and the kinematics and structural style of the evolving fold and 400 thrust belt (Table 1).

Overall, models 2 and 3 produced close to similar basin-platform geometries by the end of the extensional phase (Fig. 6a-b and 6d-e) and the curvature of the thrust fronts in map-view aligns to the orientation of the platform-basin boundary between western platform and eastern basin when increasing obliquity (compare Fig. 6a-b for 10° obliquity with Fig. 6d-e for 20° obliquity). Compared to model 1, the deviation of the strike of contractional faults across platform-basin transitions from the 405 overall strike of the model orogen is ~40° for model 2 and ~30° for model 3 (e.g., thrusts 5 of model 2 and 3 shown in Fig. 6a-b and Fig. 6d-e, respectively). Thus, higher angles between basin axes and shortening direction, lead to less curvature of the thrust front relative to the overall strike of the mountain belt (e.g., ~30° for model 3 versus ~55° for model 1).

Different to model 1, platform thrusts of models 2 and 3 preferentially link with basin thrusts at the eastern border of the grabens (Fig. 6a-b, d-e). Therefore, the location of lateral ramps and transfer zones shifts in oblique basin inversion models 410 further towards the platform-basin transition. Additionally, the difference of wavelengths of thrusts between platform and basinal areas is more pronounced in experiments with oblique basin inversion (compare Fig. 5g with Fig. 6c, f). The wavelength of thrusts is, e.g., for platform hosted thrusts 5 to 7 of model 2 (western platform, Fig. 6a-b, cross-section a-a' in Fig. 6c) is 12 cm, whereas it is only 0.8 cm for basin hosted thrusts 6 to 7 (eastern basin, cross-section b-b' in Fig. 6c). Model 3 shows comparable differences in wavelength of thrusts from platforms and basins, e.g., 7 cm for platform hosted thrusts 3 to 5 415 (western platform, Fig. 6d-e, cross-section a-a' in Fig. 6f) and 1 cm for basin hosted thrusts 4 to 5 (eastern basin, cross-section f-f' in Fig. 6f). In model 2 and model 3, ramps and especially flats of thrusts on platforms are longer (e.g., 5 cm ramp length of thrust 5 of model 2 in cross-section a-a' in Fig. 6c and 4 cm ramp length of thrust 5 of model 3 in cross-section e-e' in Fig.

6f) compared to thrusts within basins (e.g., 4 cm ramp length of thrust 7 of model 2 in cross-section b-b' in Fig. 6c and 3 cm ramp length of thrust 8 of model 3 in cross-section f-f' in Fig. 6f).

420

[Figure 6]

Models with oblique basin inversion seem to favour the development of laterally shorter (thrust sheets III and IV in model 2 in Fig. 6a-b and thrust sheets III and IV in model 3 in Fig. 6d-e) and isolated thrust systems (thrust sheet II in model 2 in Fig.

425 6a-b and thrust sheet II in model 3 in Fig. 6d-e). Model 2 (Fig. 6a-c) and model 3 (Fig. 6d-f) both show an initial thrust system I, which was laterally continuous over the entire model width, comparable to model 1 (Fig. 5). However, thrust system II of models 2 and 3 is limited to the transition of the eastern basin to the western platform only. Although very narrow in N-S direction within the eastern basin, thrust system III in model 2 extends over the entire width of the model (Fig. 6a-c), whereas thrust system IV in model 3 terminates within the eastern basin and does not reach the eastern platform (Fig. 6d-f). Also, thrust 430 sheets IV and V in model 2 (Fig. 6a-c) and thrust sheet III in model 3 (Fig. 6d-f) terminate within the eastern basin, either as western or eastern termination. This is in contrast with parallel basin inversion, where thrust systems I to III are laterally continuous along the entire model width.

In the case of oblique basin inversion, parts of platform sequences get thrust over basinal sequences as shown at the transition of the western platform to the eastern basin along thrust 7 of model 2 (Fig. 6a-b) or thrust 5 of model 3 (Fig. 6d-e). Additionally,

435 parts of basinal sequences get thrust over platform sequences (thrust 4 in cross-section c-c' in Fig. 6c, thrust 8 in cross-section f-f' and thrust 5 in cross-section g-g' in Fig. 6f). Otherwise, thrust faults cross-cut pre-existing normal faults and either overthrust them and/or transport them piggy back. In model 2, pre-existing normal faults are mostly cross-cut by younger thrust faults throughout the experiment, with an exception within the imbricated stack of thrusts of the eastern basin, where pre-existing normal faults get reactivated in oblique slip mode (thrusts 4, 6-7 in cross-section b-b' and thrusts 5 and 7 in cross-440 section c-c' in Fig. 6c). Thrusts 4, 6 and 7 of cross-section b-b' (Fig. 6c) and thrusts 5 and 7 of cross-section c-c' (Fig. 6c) of model 2 incorporate fully reactivated normal faults up to their initial termination at the boundary between syn- and post-rift sediments (cross-section d-d' in Fig. 6c) and cut through post-rift sediments to the model surface. Thrusts 6 and 7 in cross-section c-c' (Fig. 6c) are, together with non-reactivated normal faults, passively steepened by the younger in-sequence fore-thrust 8 (cross-section c-c' in Fig. 6c). Compared to model 2, oblique reactivation of pre-existing normal faults as thrust faults 445 is more common further in the hinterland of the model 3 orogen (thrusts 5-6 in cross-section f-f' and thrust 5 in cross-section g-g' in Fig. 6f). Furthermore, in model 3, normal faults are if reactivated, fully reactivated as compressional faults (e.g., thrusts 5-6, 8 in cross-section f-f' and thrusts 4 and 7 in cross-section g-g' in Fig. 6f), and cross-cut by younger back-thrusts (e.g., thrust 9 in cross-section g-g' in Fig. 6f). Overall, in oblique inversion models, pre-existing normal faults are favoured areas 450 where deformation localises (e.g., thrust 7 in cross-section g-g' in Fig. 6f grows towards the pre-existing normal fault and reactivates it), compared to parallel inversion models.

For inferring oblique slip on thrust faults, zoom-ins on the strain type and time evolution diagrams of the incremental and cumulative strain types of selected points of models 2 and 3 are provided in Fig. 7. For model 2, points (a) and (b) (upper left-hand panel in Fig. 7) are positioned in the footwall of the thrust fronts of thrust systems II and III within the eastern basin, respectively. The evolution of the two principal stretches λ (Hencky strains) shows increasing shortening at the thrust front after 50 min in model time for point (a) and slightly later (80 min) for point (b) (middle column in Fig. 7a-b). The dominant strain type for both points (a) and (b) is shortening (dilatation < 1 , see right column in Fig. 7a-b), but the incremental strain type plots in between strike-slip and shortening/extension (right column in Fig. 7a-b), indicating transpressive to transtensive motion along the thrusts. For point (a), the temporal evolution of the incremental strain type deciphers a change from thrusting to strike-slip to extension (right column of Fig. 7a); for point (b) transpression until approximately 140 min in model time, leading into pure shortening. Compared to model 2, points (c) and (d) of model 3 (middle left-hand panel in Fig. 7), which are positioned at the thrust fronts of thrust systems II and IV within the eastern basin, respectively, show shortening as dominant strain type with increased oblique slip motion of point (c) towards the end of the model run.

[Figure 7]

465

4.2.2 Influence of basal décollement rheology

Models 4-7 comprise set 2 of our experiments and focus on the influence of basal décollement rheology (Table 1) for conditions of parallel (models 4 and 6) and oblique (models 5 and 7) inversion. Variations of basal décollement strengths for parallel inversion setups (models 4 and 6, Table 1) have been included for completeness but will not be discussed in detail because of 470 less relevance for the natural example. Instead, we focus on models with an obliquity of 20° between pre-existing structures and the shortening direction, and a variation of basal décollement strength and behaviour.

The modelling results highlight major differences related to the number of thrust sheets forming and the style of fault reactivation. Model 5 (Fig. 8a-c) is characterized by a frictional and model 7 (Fig. 8d-e) by a viscous décollement below the brittle crust. The latter has the same thickness as set 1 experiments (Table 1). In both models the thickness of the décollement 475 is 0.6 cm and the platform-basin thickness ratio ranges between 0.7 and 0.8 (i.e., underfilled basin) (Table 1, Fig. 4). Notably, phase 1 extensional basins are wider and more normal faults developed in case of a viscous décollement (compare cross-section c-c' of Fig. 8c with cross-section f-f' of Fig. 8f). As such, normal faults reach further into the platforms (e.g., western platform in Fig. 8d-e), are mostly parallel, in some instances curved, and offset across strike through relay ramps (Fig. 8d-e). Upon shortening, model 5 (Fig. 8a-b) and model 7 (Fig. 8d-e) show curved thrust fronts in map-view. At an early stage of 480 deformation (i.e., thrust sheet I of model 5 and 7, Fig. 8a-b, d-e), the thrust front undulates but is approximately at the same distance from the backstop, at the platform as well as basin areas. At the final stage of deformation, the thrust front steps back in basinal areas and is located further towards the foreland on platforms (Fig. 8a-b, d-e). Thrust curvature shows maximum alignment to the orientation of basin boundaries at angles of ~30° with respect to the overall strike of the orogen (Fig. 8a-b, d-

485 e). Deformation is consistently concentrated at eastern borders of the respective basins, independent of basal décollement material (Fig. 8a-b, d-e). This is shown by obliquely striking thrusts evolving on the eastern platform which connect with thrusts in the basin through lateral ramps as indicated in the cumulative strain maps, which show predominance of compressional deformation (Fig. 8b and 8e).

490 [Figure 8]

495 However, we also find indications for incremental oblique slip movements in zoom-ins of the strain type and time evolution diagrams for selected points of models 5 and 7 (Fig. 9). For model 5, points (a) and (b) (upper left-hand panel in Fig. 9) are positioned in the footwall of the thrust front of thrust system II. The actual thrust front location is shown through areas of strongest convergence of black material lines in the zoom-in panels of the strain type (left column in Fig. 9a-b). The evolution of the two principal stretches shows increasing shortening at the thrust front after 115 min in model time for point (a) and slightly earlier (105 min) for point (b) (middle column in Fig. 9a-b), which is located closer to the moving wall and within the eastern basin where the model crust is thinner compared to the platform. The dominant strain type for both points (a) and (b) is shortening (dilatation < 1 , see right column in Fig. 9a-b), but the incremental strain type for point (b) plots in between strike-slip and shortening (right column in Fig. 9b), suggesting lateral variations in oblique slip along the thrust front of thrust system II and slightly higher oblique slip within the eastern basin (towards the eastern platform). Differences in fault kinematics are also observed at the thrust front of model 7 (points (c) and (d) in the middle left-hand panel in Fig. 9). There, point (d), located at the footwall of the frontal thrust of thrust system II, describes most of the time pure strike-slip motion (right column in Fig. 9d). Instead, point (c), located on the western platform, shows mostly shortening, with incremental strain types characterised by strike-slip and shortening (Fig. 9c).

500 505 When using glass beads or a viscous layer as basal décollement, two major thrust systems (Fig. 8) instead of three (model 1, Fig. 5) or four to five thrust systems (model 2 and model 3, Fig. 6) form. Both model 5 and model 7 show an initial thrust system I with a W-E strike covering the entire width of the models. Thrust system II of model 5 has its eastern termination within the eastern basin, whereas thrust system II of model 7 extends from the western basin towards the eastern platform. In map view, the style of deformation and thrust system evolution of model 7 is comparable to that of model 3 (Fig. 6d-e), but 510 with longer (by ca. 1 cm) ramps and flats (compare cross-sections in Figs. 6 and 8).

515 In cross-sectional view, normal faults dip shallower and are slightly more listric favouring their reactivation particularly at very low dip angle, mostly along W-dipping faults, and in fault segments close to the backstop where the orogen is at maximum height (thrusts 1-5, 7 in cross-section b-b' in Fig. 8c). Examples of fault reactivation include the lowest fault segment of thrusts 1 and 3-5 in model 5 (cross-section b-b' in Fig. 8c) and the lowest fault segment of thrust 5 in model 7 (cross-section e-e' in Fig. 8f). Compared to brittle-only models, in basin areas of models 5 and 7, where the décollements are thinned most, less listric faults are observed opposing their reactivation. Often normal faults get folded and cross-cut by thrust faults as their dip

angle mostly exceeds 45° and their dip direction varies between W- and E-dipping (cross-section b-b' in Fig. 8c and cross-section e-e' in Fig. 8f).

520

[Figure 9]

For model 7, the area of deformation affected by shortening is comparable to brittle-only models, but the viscous layer facilitates transfer of deformation to the external part of the thrust system where inversion of normal faults takes place (e.g., in the footwall of fore-thrust 5 in cross-section e-e' in Fig. 8f). Other than in brittle-only models, where deformation jumps 525 towards the foreland when a specific thickness of the thrust sheet is reached, in model 7 shear zones close to the backstop within the ductile layer lead to repeated reactivation of thrust sheet I (thrust 1 in cross-section d-d' in Fig. 8f, thrusts 1-4 in cross-section e-e' in Fig. 8f). Imbrication within the thrust sheet I and simultaneous growth of the orogen yields extensional 530 cumulative strain at the surface (Fig. 8e). In general, thrusts of set 2 experiments evolved in-sequence, with a vergence varying from mostly pop-up structures using a ductile layer (cross-sections d-d', e-e' in Fig. 8f) to foreland-directed using glass beads as basal detachment (cross-sections a-a', b-b' in Fig. 8c).

4.2.3 Influence of basin fill rheology

In models 8-10 of set 3, the basin fill consists of either quartz sand, feldspar sand or glass beads (Table 1), and oblique shortening conditions apply. Models 11 and 12 of set 3, with glass beads as basin fill and parallel inversion, will not be 535 discussed in detail. Models 8-10 show that a platform-basin thickness ratio of 1 basically leads to smaller differences in wavelengths of deformation on platforms and in basins compared to experiments with platform-basin thickness ratios of 0.7 to 0.8 (Table 1, model 1 in Fig. 5, models 2 and 3 in Fig. 6, models 5 and 7 in Fig. 8).

For models 9 and 10, lateral differences in thrust orientations (e.g., curved fore-thrust 5 in model 9 in Fig. 10d-e and 4 in model 10 in Fig. 10g-h) are similar to other oblique inversion models yet the maximum curvature at platform-basin transitions being at slightly lower angles (~25°) with respect to the overall strike of the mountain belt (e.g., model 10, Fig. 10g-h). In contrast, 540 in models where the basin fill has the same properties as the platform and is of equal thickness (model 8, Fig. 10a-b) thrusts do not change their orientation across platform boundaries (Fig. 10a-c). This suggests that the strength drop along the normal faults is not sufficient to produce changes in thrust orientation but additional lateral strength contrasts are needed as provided by a weaker basin fill. In model 8, ramps of thrust faults show similar length-scales of ca. 4 cm on platforms and in basins (thrust 8 in cross-section a-a' of Fig. 10c or thrust 10 in cross-section b-b' in Fig. 10c), whereas flat parts of thrust faults are 545 slightly shorter (by ca. 1 cm) in basinal realms.

[Figure 10]

In set 3 experiments, deformation localises at the position of pre-existing normal faults and contractional faults grow from 550 there (e.g., thrusts 1-6 in cross-section b-b' in Fig. 10c, thrusts 1-8 in cross-section f-f' in Fig. 10f, thrusts 1-9 in cross-section j-j' in Fig. 10i). Concentration of deformation appears again preferred at eastern borders of basins, i.e., where thrust faults of the younger deformation phase interact with and partly reactivate pre-existing, mostly W-dipping, normal faults (e.g., thrust 555 faults 5-8 in cross-section f-f' in Fig. 10f or thrust faults 4, 6, 8, 10 in cross-section j-j' in Fig. 10i). Normal faults of model 8 dip slightly steeper and are mostly cross-cut by thrusts (e.g., by fore-thrusts 1 to 6 in cross-section b-b' or by fore-thrusts 7-8 in cross-section c-c' in Fig. 10c). The lower friction coefficient of glass beads leads to shallower (average of 55°) dipping 555 normal faults (model 10; cross-sections j-j', i-i', k-k' in Fig. 10i). However, this does not lead to more reactivation of normal faults. In contrast, fault reactivation is most prominent in model 9 (cross-sections f-f' and g-g' in Fig. 10f), where fully reactivated normal faults reach the model surface within thrust system II (thrusts 6-8 in cross-section g-g' in Fig. 10f). Overall, pronounced foreland transport along major thrust faults (i.e., a wider orogen in N-S direction, compare cross-section 560 i-i' in Fig. 10i with cross-sections e-e' in Fig. 10f and a-a' in Fig. 10c) is the characteristic mechanism for models incorporating glass beads as basin fill (Fig. 10g-i), where the growth of the orogen in height is lower compared to models 8 and 9. Fault reactivation and orogen growth in height are the dominating mechanisms when using feldspar sand as basin fill (model 9; Fig. 10d-f). The overall deformation is in-sequence and mostly foreland directed when using glass beads and feldspar sand but using quartz sand as basin fill leads to a combination of foreland directed thrusts and pop-up structures.

565 5 Discussion of modelling results

In the following sections, we summarise (Fig. 11) and discuss the experimental results and compare them with previous studies.

5.1 Summary of modelling results

Our experiments show that the style and orientation of contractional structures are strongly affected by the inherited rift 570 geometry and the rheology of the basin fill. In particular, orientations of thrust fronts vary laterally across the inherited structures in all models, except for model 8 (Fig. 10a-b), where there is effectively no strength difference between platforms and basins at the onset of shortening. A reduction of strength along first phase normal faults is in these cases insufficient to influence the orientation of the evolving thrust structures. The analysis of incremental strain shows that oblique slip along thrust faults and reactivated normal faults predominantly occurs across platform boundaries where the strike of contractional faults deviates from the overall strike of the mountain belt by ca. ~30° (e.g., Figs. 7 and 9). 575 Models where shortening was oblique to the rift axes (10 and 20 degrees) and the platform-basin thickness ratios were less than 1 show (i) a shift of the transfer zone faults connecting platforms with basin realms from basin centers (e.g., parallel inversion of model 1 in Fig. 5) to platform-basin transitions, and (ii) a marked variability of thrust strikes of down to ~25° with respect to the overall strike of the mountain belt (compared to an average of 55° for parallel inversion models). Additionally, oblique shortening favours the reactivation of W-dipping normal faults (e.g., normal faults 4, 6-7 in cross-section b-b' in Fig.

580 6c, normal faults 4 and 7 in cross-section g-g' in Fig. 6f) whereas E-dipping normal faults are preferentially cut by contractional structures leading to thrusting of platforms on top of basin sequences and an increase of ramp lengths. Ramps and flats are especially shorter in basins in parallel inversion models as basins consist initially of thinner crust (e.g., compare cross-section b-b' of parallel inversion model 1 in Fig. 5g with cross-section b-b' of oblique (10°) inversion model 2 in Fig. 6c).
585 Models including a frictional basal décollement result in (i) shallower dipping normal faults with an average dip of 55° compared to models without (average dip of 63°), (ii) fewer thrust systems (two instead of three or more in models without basal décollement), (iii) longer ramps and flats especially on platforms, and (iv) fewer back-thrusts. Models with a viscous basal décollement show (i) curved normal faults with relay ramps in between fault segments, (ii) deformation being distributed over larger areas, (iii) fault reactivation at distance to the model orogen (e.g., reactivated normal fault in the footwall of fore-thrust 5 in cross-section e-e' in Fig. 8f), and (iv) fewer thrust systems similar to models with a frictional basal décollement.
590 Models with platform-basin thickness ratios of 1 and variable material for the basin fill (i.e., other than quartz sand) result in (i) more thrusts (Fig. 10f and Fig. 10i), (ii) more fault reactivation within basins during oblique (20°) inversion (e.g., model 3 in Fig. 6d-f and models 5 and 7 in Fig. 8), and (iii) less lateral variation in thrust orientation across platform-basin boundaries.

[Figure 11]

595

5.2 Do inherited extensional structures trigger strain localisation during contraction?

Basins in general, as well as normal faults at platform borders, represent natural weakness zones in which deformation localises during parallel to oblique basin inversion (Doglioni, 1992; Munteanu et al., 2013). Results of all models presented in this study confirm that deformation localises in areas of lateral strength contrasts in the crust such as transitions from platforms to basins, 600 which are characterised by intense faulting and a change from basement or platform to basin sequences (Figs. 5, 6, 8, 10, 11). Upon faulting, friction decreases within the quartz sand by about 17 % (Willingshofer et al., 2018). Furthermore, ring shear tests constrain fault reactivation for the analogue material for friction coefficients of ca. 0.52. For such values reactivation of normal faults dipping at 60° is expected (Sibson, 1995), leading to localisation of deformation at the position of the normal faults. However, we do not find a correlation between strain localisation and the position of the normal faults in cases where 605 there is no strength contrast from platform to basin fill, suggesting that the reduction of strength along the normal faults in our experiments is insufficient to trigger strain localisation. Instead, our modelling results suggest that lateral strength variations related to the transition from rigid platforms to the weak basin fill are required for strain to localise at platform-basin transitions. These results are consistent with earlier modelling studies demonstrating the importance of strength variations in the crust for the localisation of deformation (Brun and Nalpas, 1996; Sokoutis and Willingshofer, 2011; Bonini et al., 2012; Calignano et 610 al., 2015; Auzemery et al., 2020).

Previous studies have furthermore shown that localisation of deformation through the reactivation of pre-existing faults, is favoured when the shortening direction is at angles smaller than 45° with respect to the strike of the inherited discontinuities

(e.g., Nalpas et al., 1995; Brun and Nalpas, 1996; Amiliba et al., 2005; Panien et al., 2005; Del Ventisette et al., 2006; Yagupsky et al., 2008; Deng et al., 2020) or the fault is substantially weakened by clay smearing (e.g., Marques and Nogueira, 2008) or elevated pore-fluid pressure (Sibson, 1995). Yet the latter is not part of our experimental work, our modelling results support these earlier findings as demonstrated by the fact that inherited normal faults are more often reactivated upon oblique inversion. Additionally, we note that normal faults dipping against the direction of shortening (W-dipping normal faults in our models) seem to be better oriented for reactivation than E-dipping normal faults (Figs. 6, 8, 10). Consequently, E-dipping normal faults are preferentially cut by newly formed thrust faults. A similar relationship has been described by Panien et al. (2005).

620 **5.3 Are the vertical motions controlled by the inherited platform-basin configuration?**

The style of thrust faulting is overall comparable on platforms and in basins and mostly in-sequence, the latter is shown as the preferred deformation style in many previous analogue modelling studies (e.g., Ellis et al., 2004; Panien et al., 2005; Deng et al., 2020). Tighter spacing of thrusts in basinal areas is mostly depending on the difference of initial crustal thickness (Mulugeta, 1988). Yet accompanied with shorter and steeper ramps, this does not lead to enhanced vertical motions within 625 basinal areas. Instead, longer ramps and flats on platforms result in higher topography. The rheology of the basal décollement however, seems to be of importance for differences in vertical motion across basin boundaries. Using, e.g., a viscous basal décollement leads to shearing within the ductile layer close to the backstop within the eastern basin of model 7 (cross-section e-e' in Fig. 8f) and therefore to strong uplift of thrust sheet I. Overall, models including a basal décollement (i.e., frictional or viscous) show less topography than models without (Liu et al., 1992; Ravaglia et al., 2006), independent of platforms or basins. 630 Our modelling setup produces large (western) and small (eastern) rift basins with average widths of 12.2 and 8.6 cm, respectively (Fig. 12a). The style and number of thrust faults are very similar in large and small basins (Fig. 10g-h) but topography evolutions differ, particularly in cases where the western platforms get thrusted onto basin successions of eastern basins (e.g., models 2 and 3 in Fig. 6, models 5 and 7 in Fig. 8, models 8-10 in Fig. 10). In these cases, more pronounced thickening of the crust results in high topography.

635

[Figure 12]

5.4 What controls the variation in strike directions of the major thrust faults?

Our analogue models emphasize strong lateral variability in thrust fault orientation across platform-basin transitions, which 640 has also been observed by Ravaglia et al. (2004); Di Domenica et al. (2014). The lateral variability of thrust fault strikes with respect to the overall strike of the model orogens varies between $\sim 55^\circ$ for parallel inversion models to $\sim 25^\circ$ for oblique inversion setups. The close correlation of these variations with the platform-basin transitions suggest causal relationships with the orientation of inherited strength variations. We also note that this feature is a robust model outcome and not applicable for the exceptional case where the basin is completely filled with material of the same strength as the platforms are made of.

645 Quantitative differences of thrust front positions from the backstop in both western and eastern basins are presented in Fig. 12b. Deformation localises in both, large and small basins, but backstepping of the thrust front is more profound in larger basins (Fig. 12b) leading to stronger variations of thrust fault orientations (Fig. 11, Fig. 12b). In other cases, where the thrust front in the large and small basin are located at equivalent distances from the backstop (e.g., models 5, 8, 10 in Fig. 12b), the thrust front is either continuous from the western to the eastern basin or an additional fore-thrust formed separately in the 650 western basin without connection towards the eastern basin (e.g., model 5 in Fig. 11i-j). Thrust fronts are at approximately the same position in basins and platforms and show little variation in orientation when the platform-basin thickness ratio is 1 and no rheologic contrasts exists between basins and platforms (e.g., model 8).

Earlier studies including strength contrasts between basins and surrounding areas by variations in crustal thickness and in basin 655 fill material yielded similar results (Nalpas et al., 1995; Panien et al., 2005) suggesting that pre-existing lateral heterogeneities within the model are a major controlling factor for the orientation of the thrust faults. As such, their nature is different to variations of thrust orientations related to lateral variation of décollement strength (Cotton and Koyi, 2000; Nieuwland et al., 2000).

Surprisingly, cumulative strain on oblique thrust segments that connect basins and platforms is of thrust-type (Figs. 7 and 9) and strike-slip dominated phases of motions are transient features during incremental stages of thrust formation and 660 displacement. We suggest, that this can be explained by strain partitioning as described in complex fault systems (Krstekanić et al., 2021; Krstekanić et al., 2022).

6 Application to polyphase deformation within the Dolomites Indenter of the eastern Southern Alps

The model outcomes show that the presence of an inherited platform-basin configuration controls the localisation and overall 665 style of deformation during the subsequent shortening phase. These first-order results of our crustal-scale analogue modelling study agree with previous studies of the Dolomites Indenter of the eastern Southern Alps, highlighting the importance of inherited Mesozoic structures on Alpine deformation (Doglioni, 1992; Schönborn, 1999; Verwater et al., 2021). Other than in previous analogue modelling studies where indenters were assumed rigid (Tapponnier et al., 1982; Ratschbacher et al., 1991; Luth et al., 2013a; Luth et al., 2013b; Krstekanić et al., 2021; Krstekanić et al., 2022), we focus on indenter internal deformation and therefore follow Sokoutis et al. (2000); Willingshofer and Cloetingh (2003); Van Gelder et al. (2017), by using a 670 deformable indenter. Kinematically, the model configuration of oblique (20°) basin inversion comes closest to SSE-directed inversion of approximately N-S striking inherited discontinuities within the Dolomites Indenter of the eastern Southern Alps. As such model 7, which also resembles the natural example of the Dolomites Indenter best on aspects of structural style of extensional structures, the overall style and kinematics of deformation related to the subsequent shortening phase, and shortening within basinal areas, has been chosen as our “best fit model” which will be used for the comparison with the natural 675 example. We remark that our crustal-scale analogue models do not account for strength variations with the platforms (e.g., mechanically stronger northern part of the Trento platform, related to the presence of the up to 2 km thick Athesian Volcanic

Complex; Bosellini et al., 2007) or the evolution of the sinistral transpressive Giudicarie fault system delimiting the Dolomites Indenter to the NW (Castellarin and Cantelli, 2000; Viola et al., 2001; Pomella et al., 2012; Verwater et al., 2021), which is beyond the scope of this study.

680

6.1 Best fit model for the Dolomites Indenter

Extensional structures of the best-fit model (model 7, Fig. 8d-f) are characterised by curved fault segments, which are connected via relay ramps. In this model, normal faulting also affected parts of the Trentino platform resulting in tilted fault geometries and half-grabens (Fig. 8d-f). These structures are in accordance with local to regional scale graben structures within 685 the platforms of the Dolomites Indenter, e.g., the Seren graben (Doglioni, 1992; Doglioni and Carminati, 2008; Sauro et al., 2013) located within the hanging wall of the Bassano-Valdobbiadene thrust and probably controlled by inherited Jurassic geometries. During subsequent shortening those graben structures partly get reactivated and inverted, both in analogue models (cross-section e-e' in Fig. 8f) as in the natural analogue (Sauro et al., 2013).

The in-sequence deformation style of the shortening phase fits well with the documented in-sequence thrust sequence of the 690 Southern Alps (Doglioni, 1992; Castellarin and Cantelli, 2000). The pop-up structure of thrust system II on the western platform of the best-fit model 7 (cross-section d-d' in Fig. 8f) is in line with, e.g., the so called Asiago (i.e., Sette Comuni) pop-up structure between the Bassano-Valdobbiadene fore-thrust and the Val di Sella back-thrust (Fig. 1b) (Barbieri, 1987; Barbieri and Grandesso, 2007) of the Trento platform. The Asiago pop-up is documented as wide box-fold becoming narrower 695 when entering the Belluno basin and ending in a transpressive structure at the transition of the Belluno basin to the Friuli platform (Doglioni, 1990, 1992). A decrease in size of the pop-up structure from the Trento platform towards the Belluno basin is also documented in the best-fit model (compare cross-sections d-d' and e-e' in Fig. 8f). Comparing the style of thrusting on the platform (cross-section d-d' in Fig. 8f) and in the basin (cross-section e-e' in Fig. 8f), ramps show shallower dips in basinal compared to platform successions, resulting in longer ramps on platforms and shorter ramps in basins. Flats in basins show 700 different positions compared to flats on platforms (lower height and closer to the backstop). This observation is in accordance with models of Doglioni (1992), where, e.g., the anticline in the hanging wall of the Bassano-Valdobbiadene thrust (Fig. 1b) is located further external on the Friuli platform (i.e., Maniago thrust in Doglioni, 1992) than within the Belluno basin (i.e., Bassano thrust in Doglioni, 1992), across the W-dipping normal fault transition zone at the transition from Friuli platform to Belluno basin. W-dipping normal faults show, according to Doglioni (1992), especial strong sinistral reactivation (e.g., W-oriented faults within the sinistral transpressive Giudicarie belt at the margin of the Trento platform towards the Lombardian 705 basin). In contrast, our models suggest strike-slip movement (mostly transpression) of (reactivated normal) faults at western boundaries of basins (i.e., along E-dipping normal faults) (Fig. 9c-d). This is in accordance with strike-slip transpressive reactivation of pre-existing structures oriented oblique to the shortening direction along lateral ramps (Schönborn, 1999), like, e.g., the Cimolais-Longarone or Tagliamento zones (Nussbaum, 2000). The Cimolais-Longarone zone (Nussbaum, 2000), e.g.,

is located within the Belluno basin, in the hanging wall of the Belluno thrust, directly north of the transfer zone of the Bassano-
710 Valdobiadane thrust from Belluno basin to Friuli platform (Fig 1b).

Our best-fit model shows stronger inversion of shallow W-dipping normal faults (e.g., thrust 5 in cross-section e-e' in Fig. 8f), whereas E-dipping normal faults have more likely been folded and/or cut by compressional structures (e.g., folded and cut normal fault in the hanging wall of fore-thrust 4 in cross-section d-d' and in the hanging wall of fore-thrust 1 in cross-section e-e' in Fig. 8f). Lateral changes in fault reactivation are common at platform-basin transitions, e.g., thrust 7 in cross-section e-e' in Fig. f, which is independent from the normal fault in its immediate footwall; the latter getting reactivated as thrust fault straight E of cross-section e-e' (Fig. 8d-e).

The overall style of compressional deformation documents variations of the (frontal) thrust orientations and of the fold axes of growth folds across lateral discontinuities (e.g., platform hosted thrust 2 in Fig. 8d-e and cross-section d-d' in Fig. 8f stepping back towards the eastern basin), the latter representing anisotropies, like lateral ramps of transfer zones in, e.g., the upper to
720 middle crust. Similar effects have been shown by Ravaglia et al. (2004), where growth folds in transfer zones produce lateral culminations in the folded structures. The style of deformation within the basinal areas of the best-fit model is especially well in line with the natural analogue when comparing the model cross-section to geological cross-sections through (i) the Venetian Alps, where platform (i.e., Trento platform) get thrusted over basinal (i.e., Belluno) successions (Doglioni, 1992; Schönborn, 1999) or (ii) the Friuli Alps, where basinal (i.e., Belluno and/or Slovenian basin) sediments are located north of platform (i.e.,
725 Friuli platform) successions and get thrusted over the latter (Kastelic et al., 2008; Ponton, 2010). Characteristic for the Friuli Alps is that the backthrust is steeply dipping to the S (Fella fault), which is cut by several N-verging thrust faults (Merlini et al., 2002; Galadini et al., 2005; Kastelic et al., 2008; Ponton, 2010; Poli and Zanferrari, 2018). In our best-fit model, the position of the fore-thrusts 1-4 (cross-section e-e' in Fig. 8f) indicates polyphase shearing within the ductile layer close to the backstop (cross-section e-e' in Fig. 8f), supporting the crustal-scale (Poli et al., 2021) high-angle backthrust in, e.g., the model
730 of Venturini (1990). As this shear zone (cross-section e-e' in Fig. 8f) does not reach the model surface, discussion about the amount of lateral (dextral referring to Merlini et al., 2002) movement along the fault is not possible.

6.2 Structural observations along the western Belluno fault of the Valsugana fault system

Polyphase deformation within the Dolomites Indenter of the eastern Southern Alps is well known through regional paleostress studies with plenty of studied sites along the whole Southern Alps, dated with a tectonic stratigraphic approach (Doglioni, 1991; Carulli and Ponton, 1992; Castellarin et al., 1992; Doglioni, 1992; Polinski and Eisbacher, 1992; Caputo, 1996; Castellarin et al., 1998; Castellarin and Cantelli, 2000; Mellere et al., 2000; Venturini and Carulli, 2002; Kastelic et al., 2008; Caputo et al., 2010; Abbà et al., 2018; Poli et al., 2021). Additionally, a detailed reconstruction of the Adria-Europe convergence path, based on the magnetic anomalies of the Atlantic Ocean by Dewey et al. (1989), presented by Mazzoli and Helman (1994), suggests similar timing and direction of convergence as observed in the paleostress reconstructions of the
740 Southern Alps and other Mediterranean areas (e.g., Fellin et al., 2005; Caputo et al., 2010).

To compare analogue modelling results with internal deformation of the Dolomites Indenter, fault slip data from existing regional studies (e.g., Caputo, 1996; Castellarin and Cantelli, 2000; Caputo et al., 2010) were compiled and supplemented with new local fault slip data and shortening directions referred from strongly folded strata from the field (Fig. 13), leading to the following main deformational phases within the Dolomites Indenter since the Late Triassic: (i) D1 – Late Triassic to Jurassic
745 W-E extension, (ii) D2 – Paleogene top SW-directed shortening, mostly thin-skinned (i.e., Dinaric phase), (iii) D3 – Miocene top S(SE)-directed shortening, mostly thick-skinned (i.e., Valsugana phase), which undulates from top S- to top SSE-directed and (iv) D4 – Pliocene to Pleistocene top E(SE)-directed shortening, mostly transpressive, and with an increasing prominence
750 towards the east (Fig. 13). A common problem within the polyphase deformed Southern Alps is, when cross-cutting relationships can not be found in the field. As this is the case for D3 in our study, shortening directions changing from top SSW- via top S- to top SSE-directed were combined. Deformation phase D4 clearly cross-cuts previous, top S-directed deformation.

[Figure 13]

755 Variations in structural style along strike of thrusts within the Dolomites Indenter were studied by collecting measurements of planar (bedding, fault planes, S-C fabrics) and linear (fault striation, fold axes) structural elements along major fault zones between Adige Valley in the west (for location see label Bozen in Fig. 1b) to the Friuli Alps in the east (for location see label FriR in Fig. 1b). Here we zoom in and present structural observations along the western segment of the Belluno thrust as a case study (Fig. 14a-b). Our spatially distributed data along major faults across the Dolomites Indenter were integrated in the
760 compilation of the main deformational phases (Fig. 13).

The Belluno thrust is part of the Valsugana fault system and represents a southern thrust splay merging with the Valsugana thrust slightly east of Borgo Valsugana (location I in Fig. 14b). The Belluno thrust was mainly active during the Miocene or later (deformation phase D3, Fig. 13) with an eventual initiation in the Late Oligocene (Vignaroli et al., 2023), has been reactivated several times (Vignaroli et al., 2020), and shows seismic activity at present (Areggi et al., 2023). The overall strike
765 of the approximately 20 km long and approximately 30° to the N dipping Belluno thrust is WSW-ESE-trending (Vignaroli et al., 2020; Zuccari et al., 2021). The hanging wall of the Belluno thrust is a S-verging fault-propagation fold (Mt. Coppolo anticline) with a sub-vertical forelimb (Vignaroli et al., 2020). The Mt. Coppolo anticline exposes Upper Triassic to Lower Jurassic shallow water carbonates (Dolomia Principale, Calcari Grigi Group), which are thrusted onto Cretaceous to Paleogene strata (Maiolica Formation, Scaglia Variegata Formation, Scaglia Rossa Formation) (D'Alberto et al., 1995).

770 In the western segment of the Belluno thrust, close to where it merges into the Valsugana thrust (Fig. 14b), fault slip data from within the footwall of the Belluno thrust shows top SSW-directed shortening, accompanied by strongly folded strata with a mean fold axis of 301/14 (I in Fig. 14a, for location of I see Fig. 14b), suggesting SSW-NNE directed shortening. Further towards the east (location II in Fig. 14b), fault slip data from within the footwall of the Belluno thrust mainly shows top S-directed thrusting, with undulations towards the SSW and the SSE (II in Fig. 14a, for location of II see Fig. 14b). Top S-

775 directed thrusting is supported by shallow plunging mean fold axes of 265/05 and 091/07 within Jurassic to Cretaceous strata in the footwall of the Belluno thrust (II in Fig. 14a, for location of II see Fig. 14b). Data from location II origin from west of major pre-existing Mesozoic discontinuities within the Trento platform and towards the western boundary of the Belluno basin, e.g., the Seren graben and the Cismon valley alignment (Sauro et al., 2013). Our data of location II (Fig. 14b) support top S-directed thrusting, although mixing of directions can not be excluded totally, as cross-cutting criteria are partly hard to discover
780 within the polyphase deformed eastern Southern Alps. Even further towards the east, where the Belluno thrust crosses the boundary from the Trento platform towards the Belluno basin (location III in Fig. 14b), fault slip data from its footwall provides thrusting directions towards SSE, accompanied by a mean fold axis of 250/22 (III in Fig. 14a, for location of III see Fig. 14b). The along strike change of shortening kinematics from top SSW- via top S- to top SSE-directed in our data can be explained by strain partitioning along the Belluno thrust.

785

[Figure 14]

6.3 Variability of deformation styles and thrust fault orientations: Implications of modelling results for the eastern Southern Alps

790 Fault geometries in map-view of the conducted physical analogue experiments (Fig. 11) show strong resemblance with the fault geometries in map-view of the natural prototype (Figs. 1b, 14b). Especially striking are the tighter spacing of thrusts in basinal areas (e.g., Belluno basin), and curved thrust fronts at platform-basin transitions. Examples of the latter include the Belluno thrust both at the transition from Trento platform to Belluno basin (Zampieri and Grandesso, 2003) as from Belluno basin to Friuli platform or the Bassano-Valdobbiadene thrust at the transition from Belluno basin to Friuli platform (Picotti et
795 al., 2022). Field observations from the eastern Southern Alps also show that the spacing of thrusts is tighter within the Belluno basin than on the Trento platform (Doglioni, 1991; Doglioni and Carminati, 2008). According to Doglioni (1991), both folds and thrusts show reduced wavelengths in basinal areas in the natural prototype, supporting the tighter spacing of thrusts in basins. Our analogue models support longer wavelengths of thrusts on platforms in contrast to shorter wavelengths in basins (Figs. 5, 6, 8, 10). Transitions between variations in wavelengths of thrusts appear at platform-basin boundaries, at so called
800 transfer zones. Our models indicate that the size of the basin (Fig. 12a) controls the width of the transfer zone and the lengths of oblique lateral ramps between platform and basin domains. Backstepping of the most external thrust front in basins compared to platforms (Fig. 11) is more distinct in the western (i.e., Lombardian) basin than in the eastern (i.e., Belluno) basin (e.g., Fig. 5c-f). The increasing amount of thrusts in basins compared to platforms is not influenced by the basin size. Our study therefore emphasises that the presence of basins representing lateral mechanical strength variations (Fig. 4b) is most
805 important for lateral variations of the deformational styles.

Field observations suggest an along strike change of shortening directions at several of the studied faults (Figs. 1b, 14b). In the case of the Belluno thrust, the shortening direction changes from top SSW to top SSE along strike (Fig. 14a-b). In map-

view (Figs. 1b, 14b), this variation in shortening direction can be noticed by means of an anastomosing strike of the thrust front. This is particularly evident at the western segment of the Belluno thrust (locations I to III in Fig. 14b) where the Belluno thrust follows the Trento platform – Belluno basin boundary. West of location II the Belluno thrust is located further towards the foreland, whereas east of location III, the Belluno thrust is located further towards the hinterland.

The incremental particle path in analogue models (e.g., time step between 15 and 20 % of bulk shortening of model 1 in Fig. 14c; time step between 10 and 15 % of bulk shortening of model 5 in Fig. 14d), captured by detailed PIV-analysis is consistent with the field observations and indicates temporal variations in movement directions (between SW to SE). The associated change in orientation of the thrust front, which coincides with platform-basin transitions, is a feature we observe in most of our parallel to oblique basin inversion models (Fig. 11) and highlight the role of pre-existing discontinuities or lateral facies juxtaposition, which are visible in the inversion strain pattern.

Field data and crustal-scale analogue modelling results strongly support previous studies by, e.g., Masetti and Bianchin (1987); Doglioni (1991, 1992); Schönborn (1999) and suggest that inherited structures together with lateral strength variations controlled by the platform-basin configuration, regulate the style of subsequent compressional deformation and are the cause of variations in shortening directions along strike of thrust faults. Our study does not question the importance of large-scale paleostress analysis of previous authors (e.g., Caputo, 1996; Castellarin and Cantelli, 2000; Caputo et al., 2010), but emphasises the role of pre-existing structures on strain partitioning along regional fault systems.

7 Conclusions

A series of crustal-scale physical analogue models was performed to investigate the effect of inherited extensional structures and lateral strength variations on the style and kinematics of younger compressional deformation, associated with parallel to oblique basin inversion. Based on our modelling results, we infer the following:

1. During inversion, strain predominantly localises in areas of lateral strength contrasts such as transitions from platforms to basins.
2. Curved thrust fronts and lateral ramps coincide with the transition from platforms to basins and are therefore controlled by rheological changes including the weakness of inherited extensional faults and the transition to the weaker basin fill. These areas, referred to as transfer zones, are the surface expression of thrust connections from platform to basin realms. Transfer zones also involve lateral changes in shortening direction along strike of individual thrust faults.
3. Reactivation of inherited normal faults is favoured for oblique shortening and predominantly occurs on fault planes dipping towards the shortening direction (i.e., the moving backstop).
4. Although compressive strain dominates, variations in thrust front orientations across platform-basin boundaries are accompanied by transient incremental oblique slip movements.

5. Spacing of in-sequence thrusts is larger on platforms and smaller in basins, which is, together with the overall style
840 of deformation, less dependent on (i) the material used for the basal décollement, (ii) the style of graben borders, or
(iii) the size of the basin, but is controlled by the presence of inherited platform-basin configuration.

With reference to the Dolomites Indenter of the eastern Southern Alps, our modelling results suggest that along strike variations
845 of thrust orientations and associated shortening directions, as among others documented for the Belluno thrust of the Valsugana
fault system, are the consequence of strain partitioning controlled by inherited structures and does not necessarily reflect
different regional deformation phases. This shows that local and temporal variabilities in thrust kinematics constrained by the
rock record can be explained by strain partitioning within a stable stress field and within a single progressive phase of
deformation.

Author contributions. AKS – Conceptualisation, Methodology, Validation, Formal analysis, Investigation, Data curation,
850 Writing – original draft, Writing – review & editing, Visualization. EW – Conceptualisation, Methodology, Validation,
Resources, Writing – original draft, Writing – review & editing, Supervision. TK – Conceptualisation, Writing – review &
editing. HO – Conceptualisation, Writing – review & editing, Supervision. HP – Funding acquisition, Conceptualisation,
Writing – review & editing, Supervision.

855 **Competing interests.** At least one of the (co-)authors is a member of the editorial board and is a guest member of the editorial
board of Solid Earth. The peer-review process was guided by an independent editor, and the authors also have no other
competing financial interests or personal relationships that could have influenced the work shown in this publication.

Acknowledgements. This research is funded by the Austrian Science Fund (FWF), project P 33272 (PI Hannah Pomella), and
860 is part of a collaboration between the Department of Earth Sciences of the Utrecht University, Netherlands and the Department
of Geology of the University of Innsbruck, Austria during the PhD project of the first author. The physical analogue
experiments were performed at the Tectonic Modelling Laboratory (TecLab) of the Utrecht University, where the first author
benefitted from the assistance of Sjaak van Meulebrouck and of helpful discussions with Eva Bakx. We thank the editor
Riccardo Reitano and gratefully acknowledge the valuable comments of Vincenzo Picotti and Pamela Jara.

865 **References**

Abbà, T., Breda, A., Massironi, M., Preto, N., Piccin, G., Trentini, T., Bondesan, A., Carton, A., Fontana, A., Mozzi, P., Surian, N., Zanoner, T., and Zampieri, D.: Pre-Alpine and Alpine deformation at San Pellegrino pass (Dolomites, Italy), *Journal of Maps*, 14, 671-679, 10.1080/17445647.2018.1536001, 2018.

Abbots, F. V.: Sedimentology of Jurassic syn-rift resedimented carbonate sandbodies, University of Bristol, Bristol, 403 pp., 1989.

870 Amiliba, A., McClay, K. R., Sàbat, F., Munoz, J. A., and Roca, E.: Analogue Modelling of Inverted Oblique Rift Systems, *Geologica Acta*, 3, 251-271, 2005.

Anderlini, L., Serpelloni, E., Tolomei, C., De Martini, P. M., Pezzo, G., Gualandi, A., and Spada, G.: New insights into active tectonics and seismogenic potential of the Italian Southern Alps from vertical geodetic velocities, *Solid Earth*, 11, 1681-1698, 10.5194/se-11-1681-2020, 2020.

875 Areggi, G., Pezzo, G., Merryman Boncori, J. P., Anderlini, L., Rossi, G., Serpelloni, E., Zuliani, D., and Bonini, L.: Present-Day Surface Deformation in North-East Italy Using InSAR and GNSS Data, *Remote Sensing*, 15, 10.3390/rs15061704, 2023.

Auzemery, A., Willingshofer, E., Yamato, P., Duretz, T., and Sokoutis, D.: Strain localization mechanisms for subduction initiation at passive margins, *Global and Planetary Change*, 195, 10.1016/j.gloplacha.2020.103323, 2020.

880 Barbieri, G.: Lineamenti tectonici degli altipiani trentini e vicentini tra Folgaria e Asiago (Prealpi venete), *Mem. Sci. Geol.*, 39, 257-264, 1987.

Barbieri, G. and Grandesso, P.: Note illustrative della carta geologica d'Italia alla scala 1:50.000, foglio 082 Asiago, Servizio Geologico d'Italia, APAT, Firenze, 135 pp., 2007.

885 Beauchamp, W., Allmendinger, R. W., Barazangi, M., Demnati, A., El Alji, M., and Dahmani, M.: Inversion tectonics and the evolution of the High Atlas Mountains, Morocco, based on a geological-geophysical transect, *Tectonics*, 18, 163-184, 10.1029/1998tc900015, 1999.

Beccaluva, L., Bianchini, G., Bonadiman, C., Coltorti, M., Milani, L., Salvini, L., Siena, F., and Tassinari, R.: Intraplate lithospheric and sublithospheric components in the Adriatic domain: Nephelinite to tholeiite magma generation in the Paleogene Veneto volcanic province, southern Alps, in: *Cenozoic Volcanism in the Mediterranean Area*, 10.1130/2007.2418(07), 2007.

890 Beccaro, P., Baumgartner, P. O., and Martire, L.: Radiolarian biostratigraphy of the Fonzaso Formation, Middle-Upper Jurassic, Southern Alps, Italy, *micropaleontology*, 48, 43-60, 2002.

Bernoulli, D. and Jenkyns, H. C.: Alpine, Mediterranean, and Central Atlantic Mesozoic Facies in Relation to the Early Evolution of the Tethys, in: *Modern and Ancient Geosynclinal Sedimentation*, 129-160, 10.2110/pec.74.19.0129, 1974.

Berra, F., Galli, M. T., Reghellin, F., Torricelli, S., and Fantoni, R.: Stratigraphic evolution of the Triassic-Jurassic succession in the Western Southern Alps (Italy): the record of the two-stage rifting on the distal passive margin of Adria, *Basin Research*, 21, 335-353, 10.1111/j.1365-2117.2008.00384.x, 2009.

895 Bertotti, G.: Early Mesozoic extension and Alpine tectonics in the western Southern Alps: The geology of the area between Lugano and Menaggio (Lombardy, Northern Italy), ETH Zürich, Zürich, 1990.

Bertotti, G., Picotti, V., Bernoulli, D., and Castellarin, A.: From rifting to drifting: tectonic evolution of the South-Alpine upper crust from the Triassic to the Early Cretaceous, *Sedimentary Geology*, 86, 53-76, 1993.

900 Bonini, M., Sani, F., and Antonielli, B.: Basin inversion and contractional reactivation of inherited normal faults: A review based on previous and new experimental models, *Tectonophysics*, 522-523, 55-88, 10.1016/j.tecto.2011.11.014, 2012.

Bosellini, A.: Lineamenti strutturali delle Alpi Meridionali durante il Permo-Trias, *Mem. Mus. St. Nat. Ven. Trid.*, 15, 1-72, 1965.

Bosellini, A., Avanzini, M., Bargossi, G. M., Borsato, A., Castiglioni, G. B., Cucato, M., Morelli, C., Prosser, G., and Sapelza, A.: Note illustrative della Carta Geologica d'Italia - Appiano foglio 026, Note illustrative della Carta geologica d'Italia, SystemCard, Roma, 184 pp., 2007.

905 Boutoux, A., Bellahsen, N., Lacombe, O., Verlaguet, A., and Mouthereau, F.: Inversion of pre-orogenic extensional basins in the external Western Alps: Structure, microstructures and restoration, *Journal of Structural Geology*, 60, 13-29, 10.1016/j.jsg.2013.12.014, 2014.

Bracène, R. and Froizon de Lamotte, D.: The origin of intraplate deformation in the Atlas system of western and central Algeria: from Jurassic rifting to Cenozoic-Quaternary inversion, *Tectonophysics*, 357, 207-226, 2002.

910 Brandner, R., Gruber, A., Morelli, C., and Mair, V.: Pulses of Neotethys-Rifting in the Permomesozoic of the Dolomites, *Geo.Alp*, 13, 7-70, 2016.

Broerse, T., Krstekanić, N., Kasbergen, C., and Willingshofer, E.: Mapping and classifying large deformation from digital imagery: application to analogue models of lithosphere deformation, *Geophys. J. Int.*, 225, 984-1017, 10.1093/gji/ggab120/6195529, 2021.

Brun, J.-P.: Deformation of the continental lithosphere: Insights from brittle-ductile models, *Geological Society, London, Special Publications*, 200, 355-370, 10.1144/gsl.Sp.2001.200.01.20, 2002.

915 Brun, J.-P. and Nalpas, T.: Graben inversion in nature and experiments, *Tectonics*, 15, 677-687, 10.1029/95tc03853, 1996.

Buchanan, P. G. and McClay, K. R.: Sandbox experiments of inverted listric and planar fault systems, *Tectonophysics*, 188, 97-115, 1991.

Buiter, S. J. H., Pfiffner, O. A., and Beaumont, C.: Inversion of extensional sedimentary basins: A numerical evaluation of the localisation of shortening, *Earth and Planetary Science Letters*, 288, 492-504, 10.1016/j.epsl.2009.10.011, 2009.

920 Buiter, S. J. H., Babeyko, A. Y., Ellis, S., Gerya, T. V., Kaus, B. J. P., Kellner, A., Schreurs, G., and Yamada, Y.: The numerical sandbox: comparison of model results for a shortening and an extension experiment, in: *Analogue and Numerical Modelling of Crustal-Scale Processes*, edited by: Buiter, S. J. H., and Schreurs, G., Geological Society London, London, 29-64, 2006.

Busetti, M., Volpi, V., Barison, E., Giustiniani, M., Marchi, M., Ramella, R., Wardell, N., and Zanolla, C.: Meso-Cenozoic seismic stratigraphy and the tectonic setting of the Gulf of Trieste (northern Adriatic), *GeoActa, Special Publication* 3, 1-14, 2010.

925 Calignano, E., Sokoutis, D., Willingshofer, E., Gueydan, F., and Cloetingh, S.: Strain localization at the margins of strong lithospheric domains: Insights from analog models, *Tectonics*, 34, 396-412, 10.1002/2014tc003756, 2015.

Caputo, R.: The polyphase tectonics of the Eastern Dolomites, Italy, *Mem. Sci. Geol.*, 48, 93-106, 1996.

Caputo, R., Poli, M. E., and Zanferrari, A.: Neogene–Quaternary tectonic stratigraphy of the eastern Southern Alps, NE Italy, *Journal of Structural Geology*, 32, 1009-1027, 10.1016/j.jsg.2010.06.004, 2010.

Carminati, E., Siletto, G. B., and Battaglia, D.: Thrust kinematics and internal deformation in basement-involved fold and thrust belts: The eastern Orobie Alps case (Central Southern Alps, northern Italy), *Tectonics*, 16, 259-271, 10.1029/96tc03936, 1997.

930 Carrera, N., Muñoz, J. A., Sábat, F., Mon, R., and Roca, E.: The role of inversion tectonics in the structure of the Cordillera Oriental (NW Argentinean Andes), *Journal of Structural Geology*, 28, 1921-1932, 10.1016/j.jsg.2006.07.006, 2006.

Carulli, G. B. and Ponton, M.: Interpretazione strutturale profonda del settore centrale Carnico-Friulano, *Studi Geologici Camerti*, Nuova Serie, 275-284, 1992.

935 Castellarin, A. and Cantelli, L.: Neo-Alpine evolution of the Southern Eastern Alps, *Journal of Geodynamics*, 30, 251-274, 2000.

Castellarin, A., Selli, L., Picotti, V., and Cantelli, L.: La tettonica delle Dolomiti nel quadro delle Alpi Meridionali Orientali, *Mem. Soc. Geol. It.*, 53, 133-143, 1998.

940 Castellarin, A., Nicolich, R., Fantoni, R., Cantelli, L., Sella, M., and Selli, L.: Structure of the lithosphere beneath the Eastern Alps (southern sector of the TRANSALP transect), *Tectonophysics*, 414, 259-282, 10.1016/j.tecto.2005.10.013, 2006.

Castellarin, A., Cantelli, L., Fesce, A. M., Mercier, J. L., Picotti, V., Pini, G. A., Prosser, G., and Selli, L.: Alpine compressional tectonics in the Southern Alps. Relationships with the N-Apennines, *Annales Tectonicae*, 6, 62-94, 1992.

945 Cerca, M., Ferrari, L., Corti, G., Bonini, M., and Manetti, P.: Analogue model of inversion tectonics explaining the structural diversity of Late Cretaceous shortening in southwestern Mexico, *Lithosphere*, 2, 172-187, 10.1130/l148.1, 2010.

Cooper, M. and Warren, M. J.: Chapter 10 - Inverted fault systems and inversion tectonic settings, in: *Regional Geology and Tectonics*, Second Edition ed., edited by: Scarselli, N., Adam, J., Chiarella, D., G., R. D., and Bally, A. W., Elsevier, 169-204, 2020.

950 Cotton, J. T. and Koyi, H. A.: Modeling of thrust fronts above ductile and frictional detachments: Application to structures in the Salt Range and Potwar Plateau, Pakistan, *GSA Bulletin*, 112, 351-363, 2000.

D'Alberto, L., Boz, A., and Doglioni, C.: Structure of the Vette Feltrine (Eastern Southern Alps), *Mem. Sci. Geol.*, 47, 189-199, 1995.

Davy, P. and Cobbold, P. R.: Experiments on shortening of a 4-layer model of the continental lithosphere, *Tectonophysics*, 188, 1-25, 1991.

955 De Zanche, V., Gianolla, P., and Roghi, G.: Carnian stratigraphy in the Raibl/Cave del Predil area (Julian Alps, Italy), *Eclogae Geologicae Helvetiae* 93, 331-347, 2000.

Del Ventisette, C., Montanari, D., Sani, F., and Bonini, M.: Basin inversion and fault reactivation in laboratory experiments, *Journal of Structural Geology*, 28, 2067-2083, 10.1016/j.jsg.2006.07.012, 2006.

Deng, H., Koyi, H. A., and Zhang, J.: Modelling oblique inversion of pre-existing grabens, *Geological Society, London, Special Publications*, 487, 263-290, 10.1144/sp487.5, 2020.

960 Dewey, J. F., Helman, M. L., Knott, S. D., Turco, E., and Hutton, D. H. W.: Kinematics of the western Mediterranean, in: *Alpine Tectonics*, edited by: Coward, M. P., Dietrich, D., and Park, R. G., 1, Geological Society, London, Special Publications, 265-283, 10.1144/gsl.sp.1989.045.01.15, 1989.

Di Domenica, A., Bonini, L., Calamita, F., Toscani, G., Galuppo, C., and Seno, S.: Analogue modeling of positive inversion tectonics along differently oriented pre-thrusting normal faults: An application to the Central-Northern Apennines of Italy, *Geological Society of America Bulletin*, 126, 943-955, 10.1130/b31001.1, 2014.

965 Doglioni, C.: Tectonics of the Dolomites (Southern Alps, Northern Italy), *Journal of Structural Geology*, 9, 181-193, Doi 10.1016/0191-8141(87)90024-1, 1987.

Doglioni, C.: Thrust tectonics examples from the Venetian Alps, *Studi Geologici Camerti*, volume speciale, 117-129, 1990.

Doglioni, C.: The Venetian Alps thrust belt, in: *Thrust tectonics*, edited by: McClay, K. R., Springer, Netherlands, 319-324, 1991.

970 Doglioni, C.: Relationships between Mesozoic extensional tectonics, stratigraphy and Alpine inversion in the Southern Alps, *Eclogae geol. Helv.*, 85, 105-126, 1992.

Doglioni, C. and Bosellini, A.: Eoalpine and mesoalpine tectonics in the Southern Alps, *Geologische Rundschau*, 76, 735-754, 1987.

Doglioni, C. and Carminati, E.: Structural styles and Dolomites field trip, *Memorie Descrittive della Carta Geologica d'Italia*, Servizio Geologico d'Italia Università La Sapienza, Roma, , 2008.

Ebbing, J.: The crustal structure of the Eastern Alps from a combination of 3D gravity modelling and isostatic investigations, *Tectonophysics*, 380, 89-104, 10.1016/j.tecto.2003.12.002, 2004.

975 Ellis, S., Schreurs, G., and Panien, M.: Comparisons between analogue and numerical models of thrust wedge development, *Journal of Structural Geology*, 26, 1659-1675, 10.1016/j.jsg.2004.02.012, 2004.

Faccenda, M., Bressan, G., and Burlini, L.: Seismic properties of the upper crust in the central Friuli area (northeastern Italy) based on petrophysical data, *Tectonophysics*, 445, 210-226, 10.1016/j.tecto.2007.08.004, 2007.

Favaro, S., Handy, M. R., Scharf, A., and Schuster, R.: Changing patterns of exhumation and denudation in front of an advancing crustal indenter, Tauern Window (Eastern Alps), *Tectonics*, 36, 1053-1071, 10.1002/2016tc004448, 2017.

980 Fellin, M. G., Picotti, V., and Zattin, M.: Neogene to Quaternary rifting and inversion in Corsica: Retreat and collision in the western Mediterranean, *Tectonics*, 24, n/a-n/a, 10.1029/2003tc001613, 2005.

Franceschi, M., Massironi, M., Franceschi, P., and Picotti, V.: Spatial analysis of thickness variability applied to an Early Jurassic carbonate platform in the central Southern Alps (Italy): a tool to unravel syn-sedimentary faulting, *Terra Nova*, 26, 239-246, 10.1111/ter.12092, 2014.

Galadini, F., Poli, M. E., and Zanferrari, A.: Seismogenic sources potentially responsible for earthquakes with $M \geq 6$ in the eastern Southern Alps (Thiene-Udine sector, NE Italy), *Geophysical Journal International*, 161, 739-762, 10.1111/j.1365-246X.2005.02571.x, 2005.

985 Giambiagi, L. B., Alvarez, P. P., Godoy, E., and Ramos, V. A.: The control of pre-existing extensional structures on the evolution of the southern sector of the Aconcagua fold and thrust belt, southern Andes, *Tectonophysics*, 369, 1-19, 10.1016/s0040-1951(03)00171-9, 2003.

Gillcrist, R., Coward, M., and Mugnier, J.-L.: Structural inversion and its controls : examples from the Alpine foreland and the French Alps, *Geodinamica Acta*, 1, 5-34, 10.1080/09853111.1987.11105122, 2015.

990 Goričan, Š., Pavšic, J., and Rozic, B.: Bajocian to Tithonian age of radiolarian cherts in the Tolmin basin (NW Slovenia), *Bull. Soc. géol. France*, 183, 369-382, 2012.

Granado, P. and Ruh, J. B.: Numerical modelling of inversion tectonics in fold-and-thrust belts, *Tectonophysics*, 763, 14-29, 10.1016/j.tecto.2019.04.033, 2019.

Granado, P., Ferrer, O., Muñoz, J. A., Thöny, W., and Strauss, P.: Basin inversion in tectonic wedges: Insights from analogue modelling and the Alpine-Carpathian fold-and-thrust belt, *Tectonophysics*, 703-704, 50-68, 10.1016/j.tecto.2017.02.022, 2017.

995 Granado, P., Thöny, W., Carrera, N., Gratzer, O., Strauss, P., and Munoz, J. A.: Basement-involved reactivation in foreland fold-and-thrust belts: the Alpine-Carpathian Junction (Austria), *Geological Magazine*, 153, 1110-1135, 10.1017/s0016756816000066, 2016.

Graveleau, F., Malavieille, J., and Dominguez, S.: Experimental modelling of orogenic wedges: A review, *Tectonophysics*, 538-540, 1-66, 10.1016/j.tecto.2012.01.027, 2012.

Handy, M. R.: The structure, age and kinematics of the Pogallo Fault Zone: Southern Alps, northwestern Italy, *Eclogae geol. Helv.*, 80, 593-632, 10.5169/seals-166017, 1987.

1000 Heberer, B., Reverman, R. L., Fellin, M. G., Neubauer, F., Dunkl, I., Zattin, M., Seward, D., Genser, J., and Brack, P.: Postcollisional cooling history of the Eastern and Southern Alps and its linkage to Adria indentation, *Int J Earth Sci*, 106, 1557-1580, 10.1007/s00531-016-1367-3, 2017.

1005 Héja, G., Ortner, H., Fodor, L., Németh, A., and Kövér, S.: Modes of Oblique Inversion: A Case Study From the Cretaceous Fold and Thrust Belt of the Western Transdanubian Range (TR), West Hungary, *Tectonics*, 41, 10.1029/2021tc006728, 2022.

Hirth, G., Teyssier, C., and Dunlap, J. W.: An evaluation of quartzite flow laws based on comparisons between experimentally and naturally deformed rocks, *International Journal of Earth Sciences*, 90, 77-87, 10.1007/s005310000152, 2001.

1010 Jozi Najafabadi, A., Haberland, C., Ryberg, T., Verwater, V. F., Le Breton, E., Handy, M. R., and Weber, M.: Relocation of earthquakes in the southern and eastern Alps (Austria, Italy) recorded by the dense, temporary SWATH-D network using a Markov chain Monte Carlo inversion, *Solid Earth*, 12, 1087-1109, 10.5194/se-12-1087-2021, 2021.

Kastelic, V., Vrabec, M., Cunningham, D., and Gosar, A.: Neo-Alpine structural evolution and present-day tectonic activity of the eastern Southern Alps: The case of the Rayne Fault, NW Slovenia, *Journal of Structural Geology*, 30, 963-975, 10.1016/j.jsg.2008.03.009, 2008.

Keim, L. and Stingl, V.: Lithostratigraphy and facies architecture of the Oligocene conglomerates at Monte Parei (Fanes, Dolomites, Italy), *Rivista Italiana di Paleontologia e Stratigrafia*, 106, 123-132, 2000.

1015 Kley, J. and Monaldi, C. R.: Tectonic inversion in the Santa Barbara System of the central Andean foreland thrust belt, northwestern Argentina, *Tectonics*, 21, 11-11-11-18, 10.1029/2002tc902003, 2002.

Kley, J., Rossello, E. A., Monaldi, C. R., and Habighorst, B.: Seismic and field evidence for selective inversion of Cretaceous normal faults, Salta rift, northwest Argentina, *Tectonophysics*, 399, 155-172, 10.1016/j.tecto.2004.12.020, 2005.

1020 Klinkmüller, M., Schreurs, G., Rosenau, M., and Kemnitz, H.: Properties of granular analogue model materials: A community wide survey, *Tectonophysics*, 684, 23-38, 10.1016/j.tecto.2016.01.017, 2016.

Krstekanić, N., Matenco, L., Stojadinovic, U., Willingshofer, E., Toljić, M., and Tamminga, D.: Strain partitioning in a large intracontinental strike-slip system accommodating backarc-convex orocline formation: The Circum-Moesian Fault System of the Carpatho-Balkanides, *Global and Planetary Change*, 208, 10.1016/j.gloplacha.2021.103714, 2022.

1025 Krstekanić, N., Willingshofer, E., Broerse, T., Matenco, L., Toljić, M., and Stojadinovic, U.: Analogue modelling of strain partitioning along a curved strike-slip fault system during backarc-convex orocline formation: Implications for the Cerna-Timok fault system of the Carpatho-Balkanides, *Journal of Structural Geology*, 149, 10.1016/j.jsg.2021.104386, 2021.

Laubscher, H.: Jura, Alps and the boundary of the Adria subplate, *Tectonophysics*, 483, 223-239, 10.1016/j.tecto.2009.10.011, 2010.

Le Breton, E., Brune, S., Ustaszewski, K., Zahirovic, S., Seton, M., and Müller, R. D.: Kinematics and extent of the Piemont-Liguria Basin – implications for subduction processes in the Alps, *Solid Earth*, 12, 885-913, 10.5194/se-12-885-2021, 2021.

1030 Liu, H., McClay, K. R., and Powell, D.: Physical models of thrust wedges, in: *Thrust Tectonics*, edited by: McClay, K. R., Chapman and Hall, London, 71-81, 1992.

Lukeneder, A.: Lithostratigraphic definition and stratotype for the Puez Formation: formalisation of the Lower Cretaceous in the Dolomites (S. Tyrol, Italy), *Austrian Journal for Earth Science*, 103, 138-158, 2010.

1035 Luth, S., Willingshofer, E., Sokoutis, D., and Cloetingh, S.: Does subduction polarity changes below the Alps? Inferences from analogue modelling, *Tectonophysics*, 582, 140-161, 10.1016/j.tecto.2012.09.028, 2013a.

Luth, S., Willingshofer, E., ter Borgh, M., Sokoutis, D., van Otterloo, J., and Versteeg, A.: Kinematic analysis and analogue modelling of the Passeier- and Jaufen faults: implications for crustal indentation in the Eastern Alps, *International Journal of Earth Sciences*, 102, 1071-1090, 10.1007/s00531-012-0846-4, 2013b.

1040 Mandl, G. W.: The Alpine sector of the Tethyan shelf - Examples of Triassic to Jurassic sedimentation and deformation from the Northern Calcareous Alps, *Mitt. Österr. Geol. Ges.*, 92, 61-77, 2000.

Marocchi, M., Morelli, C., Mair, V., Klötzli, U., and Bargossi, G. M.: Evolution of Large Silicic Magma Systems: New U-Pb Zircon Data on the NW Permian Athesian Volcanic Group (Southern Alps, Italy), *The Journal of Geology*, 116, 480-498, 10.1086/590135, 2008.

Marques, F. O. and Nogueira, C. R.: Normal fault inversion by orthogonal compression: Sandbox experiments with weak faults, *Journal of Structural Geology*, 30, 761-766, 10.1016/j.jsg.2008.02.015, 2008.

1045 Martinelli, M., Franceschi, M., Massironi, M., Rizzi, A., Salvetti, G., and Zampieri, D.: An extensional syn-sedimentary structure in the Early Jurassic Trento Platform (Southern Alps, Italy) as analogue of potential hydrocarbon reservoirs developing in rifting-affected carbonate platforms, *Marine and Petroleum Geology*, 79, 360-371, 10.1016/j.marpetgeo.2016.11.002, 2017.

Masetti, D. and Bianchin, G.: Geologia del gruppo della Schiara (Dolomiti Bellunesi), *Memorie di Scienze Geologiche*, 39, 187-212, 1987.

1050 Masetti, D., Fantoni, R., Romano, R., Sartorio, D., and Trevisani, E.: Tectonostratigraphic evolution of the Jurassic extensional basins of the eastern southern Alps and Adriatic foreland based on an integrated study of surface and subsurface data, *AAPG Bulletin*, 96, 2065-2089, 10.1306/03091211087, 2012.

Masetti, D., Figus, B., Jenkyns, H. C., Barattolo, F., Mattioli, E., and Posenato, R.: Carbon-isotope anomalies and demise of carbonate platforms in the Sinemurian (Early Jurassic) of the Tethyan region: evidence from the Southern Alps (Northern Italy), *Geological Magazine*, 154, 625-650, 10.1017/s0016756816000273, 2017.

1055 Massari, F. and Neri, C.: The infill of a supradetachment(?) basin: the continental to shallow-marine Upper Permian succession in the Dolomites and Carnia (Italy), *Sedimentary Geology*, 10, 181-221, 1997.

Mattioni, L., Sassi, W., and Callot, J.-P.: Analogue models of basin inversion by transpression: role of structural heterogeneity, *Geological Society, London, Special Publications*, 272, 397-417, 10.1144/gsl.sp.2007.272.01.20, 2007.

1060 Mazzoli, S. and Helman, M.: Neogene patterns of relative plate motion for Africa-Europe: some implications for recent central Mediterranean tectonics, *Geologische Rundschau*, 83, 464-468, 1994.

Mellere, D., Stefani, C., and Angevine, C.: Polyphase Tectonics through subsidence analysis: the Oligo-Miocene Venetian and Friuli Basin, north-east Italy, *Basin Research*, 12, 159-182, 10.1046/j.1365-2117.2000.00120.x, 2000.

Mencos, J., Carrera, N., and Muñoz, J. A.: Influence of rift basin geometry on the subsequent postrift sedimentation and basin inversion: The Organjà Basin and the Bóixols thrust sheet (south central Pyrenees), *Tectonics*, 34, 1452-1474, 10.1002/2014tc003692, 2015.

1065 Merlini, S., Doglioni, C., Fantoni, R., and Ponton, M.: Analisi strutturale lungo un profilo geologico tra la linea Fella-Sava e l'avampaese adriatico (Friuli Venezia Giulia-Italia), *Mem. Soc. Geol. It.*, 57, 293-300, 2002.

Morelli, C., Bargossi, G., Mair, V., Marocchi, M., and Moretti, A.: The lower Permian volcanics along the Etsch valley from Meran to Auer (Bozen), *Mitt. Österr. Min. Ges.*, 153, 195-218, 2007.

1070 Moulin, A. and Benedetti, L.: Fragmentation of the Adriatic Promontory: New Chronological Constraints From Neogene Shortening Rates Across the Southern Alps (NE Italy), *Tectonics*, 37, 3328-3348, 10.1029/2018tc004958, 2018.

Mulugeta, G.: Modelling the geometry of Coulomb thrust wedges, *Journal of Structural Geology*, 10, 847-859, 1988.

Munteanu, I., Willingshofer, E., Sokoutis, D., Matenco, L., Dinu, C., and Cloetingh, S.: Transfer of deformation in back-arc basins with a laterally variable rheology: Constraints from analogue modelling of the Balkanides–Western Black Sea inversion, *Tectonophysics*, 602, 223-236, 10.1016/j.tecto.2013.03.009, 2013.

1075 Muttoni, G., Kent, D. V., Garzanti, E., Brack, P., Abrahamsen, N., and Gaetani, M.: Early Permian Pangea 'B' to Late Permian Pangea 'A'*, *Earth and Planetary Science Letters*, 215, 379-394, 10.1016/s0012-821x(03)00452-7, 2003.

Nalpas, T., Le Douaran, S., Brun, J. P., Unternehr, P., and Richert, J.-P.: Inversion of the Broad Fourteens Basin (offshore Netherlands), a small-scale model investigation, *Sedimentary Geology*, 95, 237-250, 1995.

1080 Nieuwland, D. A., Leutscher, J. H., and Gast, J.: Wedge equilibrium in fold-and-thrust belts: prediction of out-of-sequence thrusting based on sandbox experiments and natural examples, *Netherlands Journal of Geosciences - Geologie en Mijnbouw*, 79, 81-91, 10.1017/s0016774600021594, 2000.

Noé, S. U.: Facies and Paleogeography of the Marine Upper Permian and of the Permian-Triassic Boundary in the Southern Alps (Bellerophon Formation, Tesero Horizon), *Facies*, 16, 89-142, 1987.

1085 Nussbaum, C.: Neogene tectonics and thermal maturity of sediments of the easternmost Southern Alps (Friuli area, Italy).pdf>, Institut de Géologie, Université de Neuchâtel, 2000.

Oswald, P., Ortner, H., and Gruber, A.: Deformation around a detached half-graben shoulder during nappe stacking (Northern Calcareous Alps, Austria), *Swiss Journal of Geosciences*, 112, 23-37, 10.1007/s00015-018-0333-4, 2018.

Pace, P., Domenica, A. D., and Calamita, F.: Summit low-angle faults in the Central Apennines of Italy: Younger-on-older thrusts or rotated normal faults? Constraints for defining the tectonic style of thrust belts, *Tectonics*, 33, 756-785, 10.1002/2013tc003385, 2014.

1090 Panien, M., Schreurs, G., and Pfiffner, O. A.: Sandbox experiments on basin inversion: testing the influence of basin orientation and basin fill, *Journal of Structural Geology*, 27, 433-445, 10.1016/j.jsg.2004.11.001, 2005.

Panien, M., Buiter, S. J. H., Schreurs, G., and Pfiffner, O. A.: Inversion of a symmetric basin: insights from a comparison between analogue and numerical experiments, in: *Analogue and Numerical Modelling of Crustal-Scale Processes*, edited by: Buiter, S. J. H., and Schreurs, G., *Special Publications*, Geological Society, London, 253-270, 2006.

1095 Picotti, V. and Cobianchi, M.: Jurassic periplatform sequences of the Eastern Lombardian Basin (Southern Alps). The deep-sea record of the tectonic evolution, growth and demise history of a carbonate platform, *Mem. Sci. Geol.*, 48, 171-219, 1996.

1096 Picotti, V. and Cobianchi, M.: Jurassic stratigraphy of the Belluno Basin and Friuli Platform: a perspective on far-field compression in the Adria passive margin, *Swiss Journal of Geosciences*, 110, 833-850, 10.1007/s00015-017-0280-5, 2017.

1100 Picotti, V., Prosser, G., and Castellarin, A.: Structures and kinematics of the Giudicarie-Val Trompia fold and thrust belt (Central Southern Alps, northern Italy), *Memorie di Scienze Geologiche*, Padova, 47, 95-109, 1995.

1105 Picotti, V., Romano, M. A., Ponza, A., Guido, F. L., and Peruzza, L.: The Montello thrust and the active mountain front of the eastern Southern Alps (northeast Italy), *Tectonics*, 10.1029/2022tc007522, 2022.

1110 Placer, L., Vrabec, M., and Celarc, B.: The bases for understanding of the NW Dinarides and Istria Peninsula tectonics, *Geologija*, 53, 55-86, 10.5474/geologija.2010.005, 2010.

1115 Poli, M. E. and Zanferrari, A.: The seismogenic sources of the 1976 Friuli earthquakes: a new seismotectonic model for the Friuli area, *Bollettino di Geofisica Teorica ed Applicata*, 59, 1-18, 10.4430/bgta0209, 2018.

1120 Poli, M. E., Monegato, G., Fontana, A., Mozzi, P., Rossato, S., Zampieri, D., Falcucci, E., Gori, S., Caputo, R., and Zanferrari, A.: Comment on "Fragmentation of the Adriatic Promontory: New Chronological Constraints From Neogene Shortening Rates Across the Southern Alps (NE Italy)" by Moulin & Benedetti, *Tectonics*, 40, 10.1029/2019TC005696, 2021.

1125 Polinski, R. K. and Eisbacher, G. H.: Deformation partitioning during polyphase oblique convergence in the Karawanken Mountains, southeastern Alps, *Journal of Structural Geology*, 14, 1203-1213, 1992.

1130 Pomella, H., Stipp, M., and Fügenschuh, B.: Thermochronological record of thrusting and strike-slip faulting along the Giudicarie fault system (Alps, Northern Italy), *Tectonophysics*, 579, 118-130, 10.1016/j.tecto.2012.04.015, 2012.

1135 Pomella, H., Kloetzli, U., Scholger, R., Stipp, M., and Fügenschuh, B.: The Northern Giudicarie and the Meran-Mauls fault (Alps, Northern Italy) in the light of new paleomagnetic and geochronological data from boudinaged Eo-/Oligocene tonalites, *International Journal of Earth Sciences*, 100, 1827-1850, 10.1007/s00531-010-0612-4, 2011.

1140 Ponton, M.: *Architettura delle Alpi Friulane*, Edizioni del Museo Friulano di Storia Naturale, Udine, 2010.

1145 Ramos, A., Fernández, O., Terrinha, P., and Muñoz, J. A.: Neogene to recent contraction and basin inversion along the Nubia-Iberia boundary in SW Iberia, *Tectonics*, 36, 257-286, 10.1002/2016tc004262, 2017.

1150 Ratschbacher, L., Merle, O., Davy, P., and Cobbold, P.: Lateral extrusion in the eastern Alps, Part 1: Boundary conditions and experiments scaled for gravity, *Tectonics*, 10, 245-256, 10.1029/90tc02622, 1991.

1155 Ravaglia, A., Turrini, C., and Seno, S.: Mechanical stratigraphy as a factor controlling the development of a sandbox transfer zone: a three-dimensional analysis, *Journal of Structural Geology*, 26, 2269-2283, 10.1016/j.jsg.2004.04.009, 2004.

1160 Ravaglia, A., Seno, S., Toscani, G., and Fantoni, R.: Mesozoic extension controlling the Southern Alps thrust front geometry under the Po Plain, Italy: Insights from sandbox models, *Journal of Structural Geology*, 28, 2084-2096, 10.1016/j.jsg.2006.07.011, 2006.

1165 Rosenberg, C. L., Brun, J. P., Cagnard, F., and Gapais, D.: Oblique indentation in the Eastern Alps: Insights from laboratory experiments, *Tectonics*, 26, n/a-n/a, 10.1029/2006tc001960, 2007.

1170 Rosenberg, C. L., Schneider, S., Scharf, A., Bertrand, A., Hammerschmidt, K., Rabaute, A., and Brun, J. P.: Relating collisional kinematics to exhumation processes in the Eastern Alps, *Earth-Science Reviews*, 176, 311-344, 10.1016/j.earscirev.2017.10.013, 2018.

1175 Rožič, B., Gerčar, D., Oprčkal, P., Švara, A., Turnšek, D., Kolar-Jurkovšek, T., Udovč, J., Kunst, L., Fabjan, T., Popit, T., and Gale, L.: Middle Jurassic limestone megabreccia from the southern margin of the Slovenian Basin, *Swiss Journal of Geosciences*, 112, 163-180, 10.1007/s00015-018-0320-9, 2018.

1180 Ruh, J. B.: Effects of fault-weakening processes on oblique intracontinental rifting and subsequent tectonic inversion, *American Journal of Science*, 319, 315-338, 10.2475/04.2019.03, 2019.

1185 Sapin, F., Ringenbach, J. C., and Clerc, C.: Rifted margins classification and forcing parameters, *Sci Rep*, 11, 8199, 10.1038/s41598-021-87648-3, 2021.

1190 Sarti, M., Bosellini, A., and Winterer, E.: Basin Geometry and Architecture of a Tethyan Passive Margin, Southern Alps, Italy: Implications for Rifting Mechanisms, in: *Geology and Geophysics of Continental Margins*, edited by: Watkins, J. S., Zhiqiang, F., and McMillen, K. J., The American Association of Petroleum Geologists, Tulsa, Oklahoma, USA, 1992.

1195 Sassi, W., Colletta, B., Balé, P., and Paquereau, T.: Modelling of structural complexity in sedimentary basins: the role of pre-existing faults in thrust tectonics, *Tectonophysics*, 226, 97-112, 1993.

1200 Sauro, F., Zampieri, D., and Filippioni, M.: Development of a deep karst system within a transpressional structure of the Dolomites in north-east Italy, *Geomorphology*, 184, 51-63, 10.1016/j.geomorph.2012.11.014, 2013.

1205 Scharf, A., Handy, M. R., Favaro, S., Schmid, S. M., and Bertrand, A.: Modes of orogen-parallel stretching and extensional exhumation in response to microplate indentation and roll-back subduction (Tauern Window, Eastern Alps), *International Journal of Earth Sciences*, 102, 1627-1654, 10.1007/s00531-013-0894-4, 2013.

1210 Schmid, S. M., Fügenschuh, B., Kissling, E., and Schuster, R.: Tectonic map and overall architecture of the Alpine orogen, *Eclogae Geologicae Helvetiae*, 97, 93-117, 10.1007/s00015-004-1113-x, 2004.

1215 Schmid, S. M., Scharf, A., Handy, M. R., and Rosenberg, C. L.: The Tauern Window (Eastern Alps, Austria): a new tectonic map, with cross-sections and a tectonometamorphic synthesis, *Swiss Journal of Geosciences*, 106, 1-32, 10.1007/s00015-013-0123-y, 2013.

1155 Schmid, S. M., Fügenschuh, B., Kounov, A., Maťenco, L., Nievergelt, P., Oberhängli, R., Pleuger, J., Schefer, S., Schuster, R., Tomljenović, B., Ustaszewski, K., and van Hinsbergen, D. J. J.: Tectonic units of the Alpine collision zone between Eastern Alps and western Turkey, *Gondwana Research*, 78, 308-374, 10.1016/j.gr.2019.07.005, 2020.

Schönborn, G.: A kinematic model of the western Bergamasco Alps, Southern Alps, Italy, *Eclogae geol. Helv.*, 83, 665-682, 10.5169/seals-166607, 1990.

Schönborn, G.: Balancing cross sections with kinematic constraints: The Dolomites (northern Italy), *Tectonics*, 18, 527-545, 10.1029/1998tc900018, 1999.

Scisciani, V., Calamita, F., Tavarnelli, E., Rusciadelli, G., Ori, G. G., and Paltrinieri, W.: Foreland-dipping normal faults in the inner edges of syn-orogenic basins: a case from the Central Apennines, Italy, *Tectonophysics*, 330, 211-224, 2001.

1160 Sellì, L.: Il lineamento della Valsugana fra Trento e Cima d'Asta: Cinematica Neogenica ed eredità strutturale Permo-Mesozoiche nel quadro evolutivo del Sudalpino Orientale (NE-Italia), *Mem. Sci. Geol.*, 53, 503-541, 1998.

Sibson, R. H.: A note on fault reactivation, *Journal of Structural Geology*, 7, 751-754, 1985.

Sibson, R. H.: Selective fault reactivation during basin inversion: potential for fluid redistribution through fault-valve action, *Geological Society, London, Special Publications*, 88, 3-19, 10.1144/gsl.Sp.1995.088.01.02, 1995.

1165 Smuc, A.: Jurassic and Cretaceous stratigraphy and sedimentary evolution of the Julian Alps, NW Slovenia, Zalozba ZRC, Lubljana, 98 pp., 2005.

Smuc, A. and Goričan, Š.: Jurassic sedimentary evolution of a carbonate platform into a deep-water basin, Mt. Mangart (Slovenian-Italian border), *Riv. It. Paleont. Strat.*, 111, 45-70, 2005.

Sokoutis, D. and Willingshofer, E.: Decoupling during continental collision and intra-plate deformation, *Earth and Planetary Science Letters*, 305, 435-444, 10.1016/j.epsl.2011.03.028, 2011.

1170 Sokoutis, D., Bonini, M., Medvedev, S., Boccaletti, M., Talbot, C. J., and Koyi, H. A.: Indentation of a continent with a built-in thickness change: experiment and nature, *Tectonophysics*, 320, 243-270, 2000.

Stampfli, G. M. and Borel, G. D.: A plate tectonic model for the Paleozoic and Mesozoic constrained by dynamic plate boundaries and restored synthetic oceanic isochrons, *Earth and Planetary Science Letters*, 196, 2002.

1175 Stampfli, G. M., Borel, G. D., Marchant, R., and Mosar, J.: Western Alps geological constraints on western Tethyan reconstructions, *Journal of the Virtual Explorer*, 8, 77-106, 2002.

Šumanovac, F., Orešković, J., and Grad, M.: Crustal structure at the contact of the Dinarides and Pannonian basin based on 2-D seismic and gravity interpretation of the Alp07 profile in the ALP 2002 experiment, *Geophysical Journal International*, 179, 615-633, 10.1111/j.1365-246X.2009.04288.x, 2009.

1180 Tapponnier, P., Peltzer, G., and Armijo, R.: On the mechanics of the collision between India and Asia, *Geological Society, London, Special Publications*, 19, 113-157, 10.1144/gsl.Sp.1986.019.01.07, 1986.

Tapponnier, P., Peltzer, G., Le Dain, A. Y., Armijo, R., and Cobbold, P.: Propagating extrusion tectonics in Asia: New insights from simple experiments with plasticine, *Geology*, 10, 611-616, 1982.

1185 Tavani, S., Mencos, J., Bausà, J., and Muñoz, J. A.: The fracture pattern of the Sant Corneli Bóixols oblique inversion anticline (Spanish Pyrenees), *Journal of Structural Geology*, 33, 1662-1680, 10.1016/j.jsg.2011.08.007, 2011.

Thielicke, W. and Stamhuis, E. J.: PIVlab – Towards User-friendly, Affordable and Accurate Digital Particle Image Velocimetry in MATLAB, *Journal of Open Research Software*, 2, 10.5334/jors.bl, 2014.

Thomas, W. A.: Controls on locations of transverse zones in thrust belts, *Eclogae geol. Helv.*, 83, 727-744, 10.5169/seals-166611, 1990.

1190 Turner, J. P. and Williams, G. A.: Sedimentary basin inversion and intra-plate shortening, *Earth-Science Reviews*, 65, 277-304, 10.1016/j.earscirev.2003.10.002, 2004.

Ustaszewski, K., Kounov, A., Schmid, S. M., Schaltegger, U., Krenn, E., Frank, W., and Fügenschuh, B.: Evolution of the Adria-Europe plate boundary in the northern Dinarides: From continent-continent collision to back-arc extension, *Tectonics*, 29, n/a-n/a, 10.1029/2010tc002668, 2010.

1195 van Gelder, I. E., Willingshofer, E., Sokoutis, D., and Cloetingh, S. A. P. L.: The interplay between subduction and lateral extrusion: A case study for the European Eastern Alps based on analogue models, *Earth and Planetary Science Letters*, 472, 82-94, 10.1016/j.epsl.2017.05.012, 2017.

van Gelder, I. E., Matenco, L., Willingshofer, E., Tomljenović, B., Andriessen, P. A. M., Ducea, M. N., Beniest, A., and Grujć, A.: The tectonic evolution of a critical segment of the Dinarides-Alps connection: Kinematic and geochronological inferences from the Medvednica Mountains, NE Croatia, *Tectonics*, 34, 1952-1978, 10.1002/2015tc003937, 2015.

1200 Venturini, C.: Cinematica Neogenico-Quaternaria del Sudalpino Orientale (Settore Friulano), *Studi Geologici Camerti*, 109-116, 1990.

Venturini, C. and Carulli, G. B.: Neoalpine structural evolution of the Carnic Alps central core (Mt. Amarina, Mt. Plauris, Mt. San Simeone), *Mem. Soc. Geol. It.*, 57, 1-9, 2002.

Venzo, S.: Studio Geotettonico del Trentino meridionale-orientale tra Borgo Valsugana e M. Coppolo, *Memorie dell' Instituto Geologico della R. Università di Padova*, 14, 1-86, 1940.

1205 Venzo, S.: I depositi quaternari e del Neogene Superiore nella bassa valle del Piave da Quero al Montello e del Paleopiatte nella valle del Soligo (Treviso), *Memorie degli Istituti di Geologia e Mineralogia dell'Università di Padova*, 30, 1-27, 1977.

Verwater, V. F., Le Breton, E., Handy, M. R., Picotti, V., Jozi Najafabadi, A., and Haberland, C.: Neogene kinematics of the Giudicarie Belt and eastern Southern Alpine orogenic front (Northern Italy), 10.5194/se-2021-19, 2021.

1210 Viganò, A. and Martin, S.: Thermorheological model for the European Central Alps: brittle?ductile transition and lithospheric strength, *Terra Nova*, 19, 309-316, 10.1111/j.1365-3121.2007.00751.x, 2007.

Vignaroli, G., Viola, G., Diamanti, R., Zuccari, C., Garofalo, P. S., Bonini, S., and Selli, L.: Multistage strain localisation and fluid-assisted cataclasis in carbonate rocks during the seismic cycle: Insights from the Belluno Thrust (eastern Southern Alps, Italy), *Journal of Structural Geology*, 141, 10.1016/j.jsg.2020.104216, 2020.

1215 Vignaroli, G., Curzi, M., Zuccari, C., Aldega, L., Billi, A., Carminati, E., Van der Lelij, R., Kylander-Clark, A., and Viola, G.: Long-term tectonic evolution of the Eastern Southern Alps (Italy): a reappraisal from new structural and radiometric constraints, *EGU General Assembly 2023*, Vienna, Austria, 24-28 Apr 2023, 10.5194/egusphere-egu23-16650, 2023.

Viola, G., Mancktelow, N. S., and Seward, D.: Late Oligocene-Neogene evolution of Europe-Adria collision: New structural and geochronological evidence from the Giudicarie fault system (Italian Eastern Alps), *Tectonics*, 20, 999-1020, 10.1029/2001tc900021, 2001.

1220 Viscolani, A., Grützner, C., Diercks, M., Reicherter, K., and Ustaszewski, K.: Late Quaternary Tectonic Activity of the Udine-Buttrio Thrust, Friulian Plain, NE Italy, *Geosciences*, 10, 10.3390/geosciences10020084, 2020.

Vlahović, I., Tišljar, J., Velić, I., and Matičec, D.: Evolution of the Adriatic Carbonate Platform: Palaeogeography, main events and depositional dynamics, *Palaeogeography, Palaeoclimatology, Palaeoecology*, 220, 333-360, 10.1016/j.palaeo.2005.01.011, 2005.

Vrabec, M., Smuc, A., Pleniar, M., and Buser, S.: Geological Evolution of Slovenia - An overview, in: *The Geology of Slovenia*, edited by: Pleniar, M., Ogorelec, B., and Novak, M., 23-40, 2009.

1225 Weijermars, R.: *Principles of Rock Mechanics*, Alboran Science Publishing, University of California, 360 pp., 1997.

Willingshofer, E. and Cloetingh, S.: Present-day lithospheric strength of the Eastern Alps and its relationship to neotectonics, *Tectonics*, 22, n/a-n/a, 10.1029/2002tc001463, 2003.

Willingshofer, E., Sokoutis, D., Beekman, F., Schönebeck, J.-M., and Rosenau, M.: Ring shear test data of feldspar sand and quartz sand used in the Tectonic Laboratory (TecLab) at Utrecht University for experimental Earth Science applications. (V. 1.) [dataset], <https://doi.org/10.5880/fidgeo.2018.072>, 2018.

1230 Winterer, E. L. and Bosellini, A.: Subsidence and Sedimentation on Jurassic Passive Continental Margin, Southern Alps, Italy, *AAPG Bulletin*, 65, 394-421, 1981.

Yagupsky, D. L., Cristallini, E. O., Fantín, J., Valcarce, G. Z., Bottesi, G., and Varadé, R.: Oblique half-graben inversion of the Mesozoic Neuquén Rift in the Malargüe Fold and Thrust Belt, Mendoza, Argentina: New insights from analogue models, *Journal of Structural Geology*, 30, 839-853, 10.1016/j.jsg.2008.03.007, 2008.

1235 Yamada, Y. and McClay, K.: Influence of shear angle on hangingwall deformation during tectonic inversion, *Island Arc*, 19, 546-559, 10.1111/j.1440-1738.2010.00731.x, 2010.

Zampieri, D.: Tertiary extension in the southern Trento Platform, Southern Alps, Italy, *Tectonics*, 14, 645-657, 1995.

1240 Zampieri, D. and Grandesso, P.: Fracture networks on the Belluno syncline, a fault-propagation fold in the footwall of the Belluno thrust, Venetian Alps, NE Italy, in: *Fracture and In-Situ Stress Characterization of Hycocarbon Reservoir*, edited by: Ameen, M., Geological Society, Special Publications, London, 101-106, 2003.

Zanchetta, S., Malusà, M. G., and Zanchi, A.: Pre-collisional development and Cenozoic evolution of the central Southern Alps (N Italy), *Rend. Online Soc. Geol. It.*, 29, 194-197, 2013.

1245 Zanchi, A., D'Adda, P., Zanchetta, S., and Berra, F.: Syn-thrust deformation across a transverse zone: the Grem-Vedra fault system (central Southern Alps, N Italy), *Swiss Journal of Geosciences*, 105, 19-38, 10.1007/s00015-011-0089-6, 2012.

Zattin, M., Cuman, A., Fantoni, R., Martin, S., Scotti, P., and Stefani, C.: From Middle Jurassic heating to Neogene cooling: The thermochronological evolution of the southern Alps, *Tectonophysics*, 414, 191-202, 10.1016/j.tecto.2005.10.020, 2006.

Zuccari, C., Vignaroli, G., and Viola, G.: Geological map of the San Donato – Costa Thrust Zone, Belluno Thrust System, eastern Southern Alps (northern Italy), *Journal of Maps*, 17, 337-347, 10.1080/17445647.2021.1946444, 2021.

1250 Zwaan, F., Schreurs, G., Buiter, S. J. H., Ferrer, O., Reitano, R., Rudolf, M., and Willingshofer, E.: Analogue modelling of basin inversion: a review and future perspectives, *Solid Earth*, 13, 1859-1905, 10.5194/se-13-1859-2022, 2022.

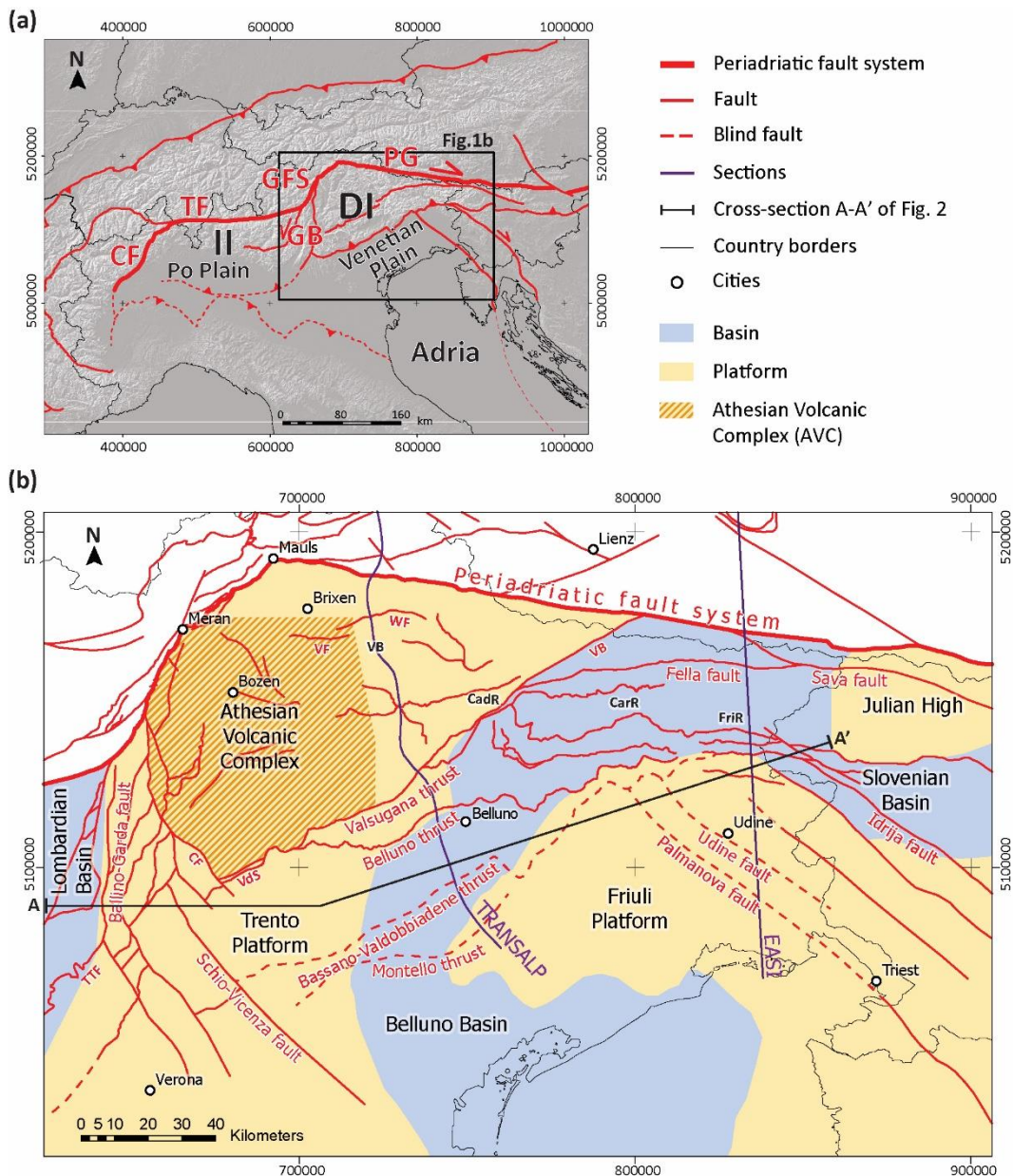
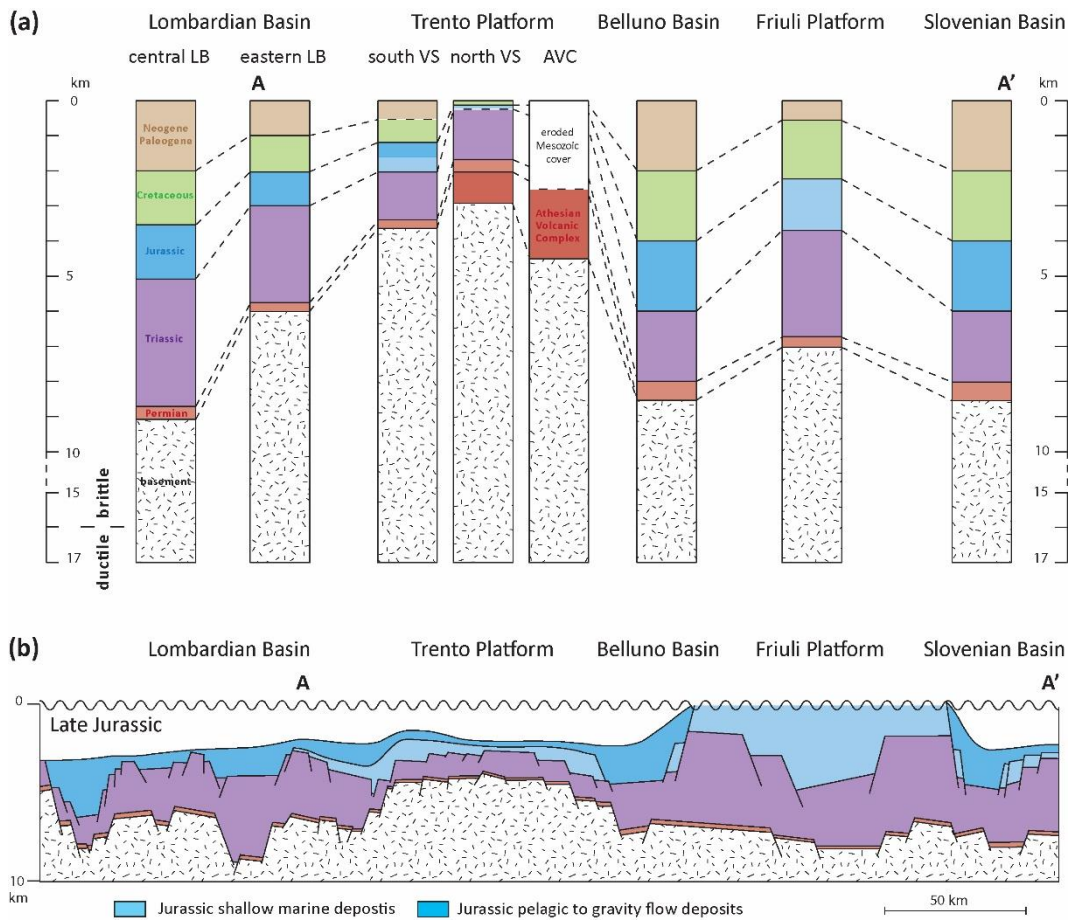
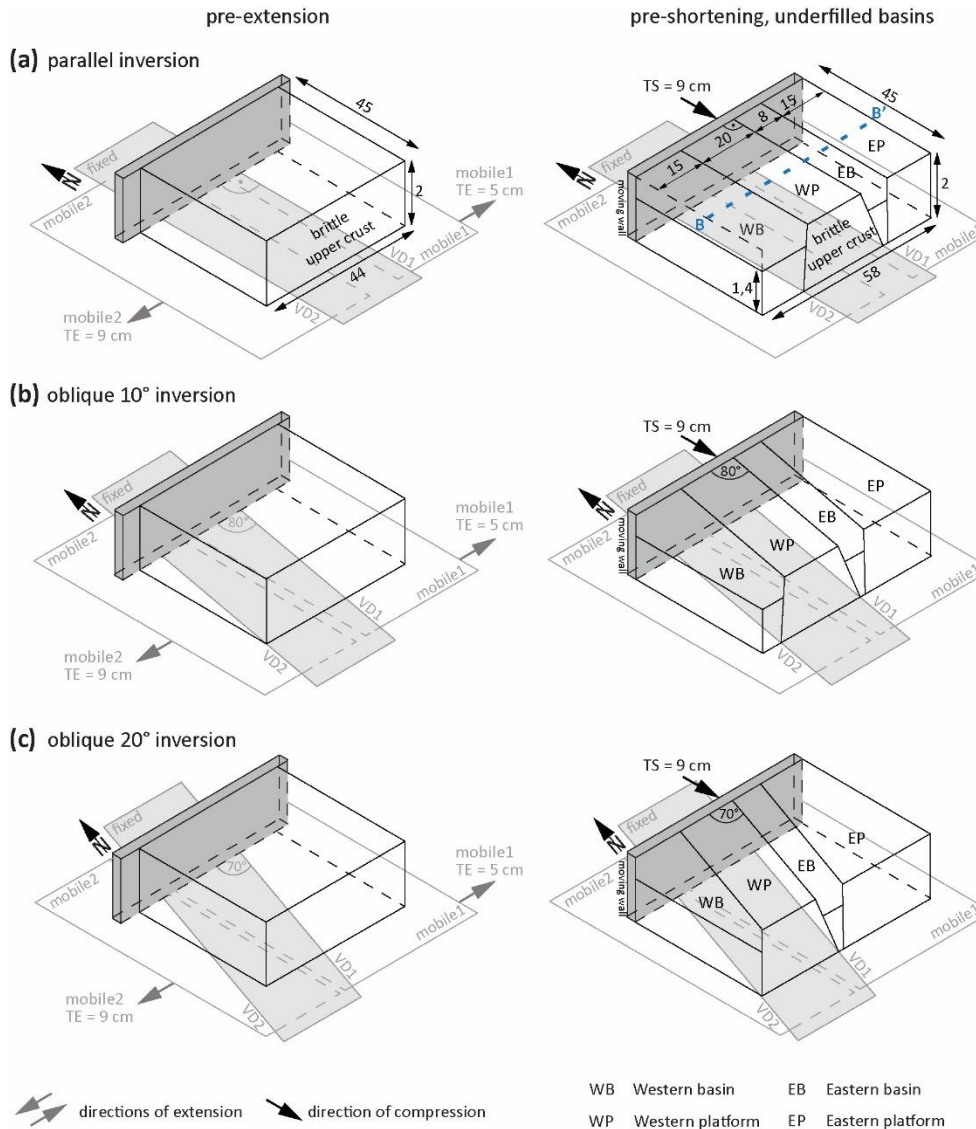


Figure 1. (a) Hillshaded digital elevation model (DEM) of the Alpine Arc of western Austria, Switzerland, northern Italy and Slovenia overlain by first-order structures of the Alpine orogen (modified from Schmid et al., 2004; 2020). The DEM was taken from the European Commission (EU-DEM). Coordinates here and in Fig. 1b are in WGS 84/UTM zones 32T and 33T. Abbreviations: PG – Pustertal-Gailtal fault, GFS – Giudicarie fault system, GB – Giudicarie belt, TF – Tonale fault, CF – Calisio fault, DI – Dolomites Indenter, II – Insubric indenter. (b) Late Triassic/Jurassic platform-basin configuration (modified from Winterer and Bosellini, 1981; Busetti et al., 2010; Masetti et al., 2012; Martinelli et al., 2017; Picotti and Cobianchi, 2017; Picotti et al., 2022) projected over the present day geography and overlain by the tectonic map of the Dolomites Indenter (modified from Schönborn, 1999; Castellarin and Cantelli, 2000; Schmid et al., 2004; Ponton, 2010; Viscolani et al., 2020). Abbreviations red: VF – Villnöss/Funes fault, WF – Würzjoch/Passo delle Erbe fault, TTF – Tremosine-Tignale fault, VB – Val Bordaglia fault, CF – Calisio fault, VdS – Val di Sella back-thrust. Abbreviations black: CadR – Cadore region, CarR – Carnia region, FriR – Friuli region, VB – Val Badia/Gadertal.



1265

Figure 2. Paleogeographic domains of the Dolomites Indenter. The location of cross-section A-A' is indicated in Fig. 1b. (a) Simplified stratigraphic columns for each paleogeographic domain (modified from Bertotti et al., 1993; Picotti et al., 1995; Picotti and Cobianchi, 2017; Verwater et al., 2021). (b) Cross-section (vertically exaggerated!) through the Jurassic platform-basin configuration (modified from Winterer and Bosellini, 1981; Smuc and Goričan, 2005).



1270 **Figure 3.** Simplified sketches of the geometric and kinematic modelling setup for brittle only models with underfilled basins (set 1, Table 1) depicting pre-extension (left panel) and pre-shortening (right panel) experimental conditions for inversion where the shortening direction is parallel to the strike of the pre-defined velocity discontinuities (a), or oblique with angles of 10° (b) or 20° (c). The eastern basin (EB) localises at VD1 due to pulling of the mobile sheet 1 below the fixed plastic sheet, whereas the western basin (WB) localises at VD2 due to pulling of mobile sheet 2. Mobile sheets 1 and 2 are pulled in a direction indicated by the grey arrows. All numbers in Fig. 3a-c without units are in centimeters. Dimensions are the same for all setups in Fig. 3a-c. Abbreviations: VD – velocity discontinuity, TE – total extension, TS – total shortening.

1275

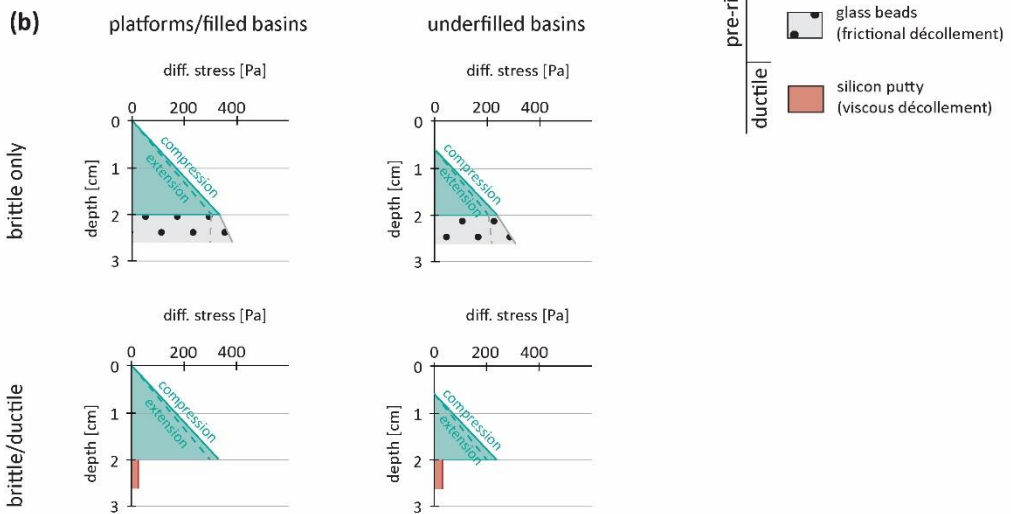
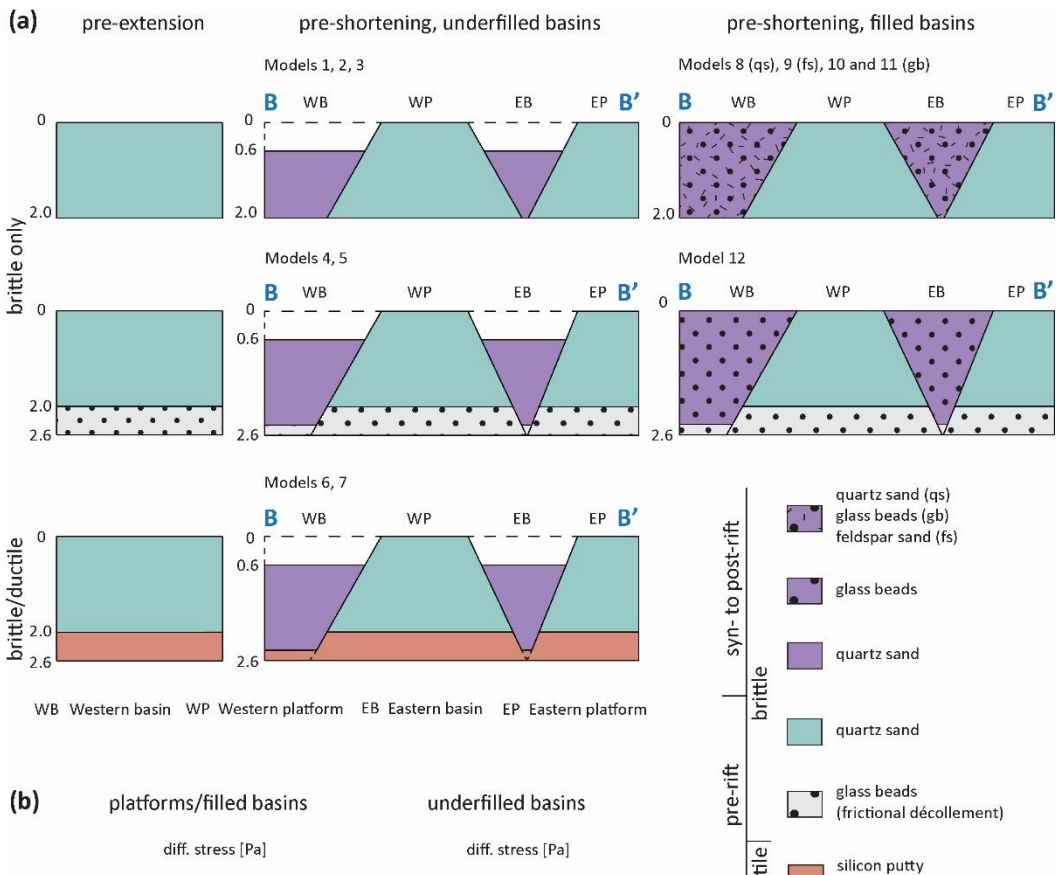


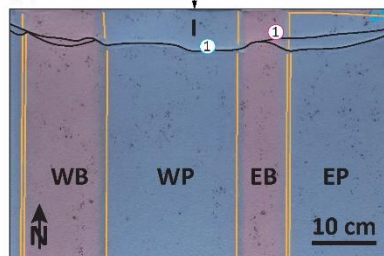
Figure 4. Modelling setup. (a) Simplified sketches of setup cross-sections for brittle only and brittle/ductile experiments. Cross-section location is indicated in Fig. 3a. (b) Strength profiles for brittle only and for brittle/ductile experiments for platforms/filled basins (platform-basin thickness ratio of 1) and for underfilled basins (platform-basin thickness ratio of 0.7 to 0.8). All numbers in Fig. 4a without units are in centimeters.

Model 1 - Reference Model

(a) post-extension/pre-shortening (0 % BS)

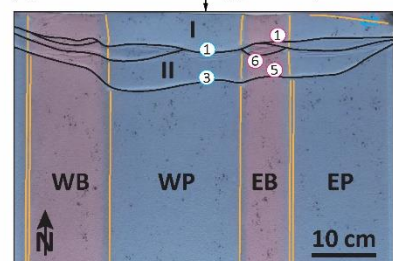


(b) 2.25 cm of shortening (5 % BS)

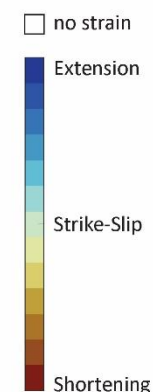
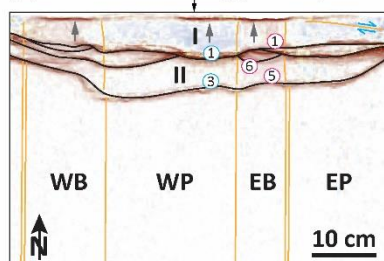


WB Western basin
WP Western platform
EB Eastern basin
EP Eastern platform

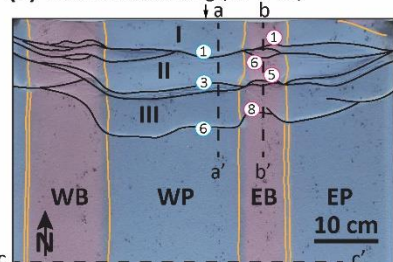
(c) 4.5 cm of shortening (10 % BS)



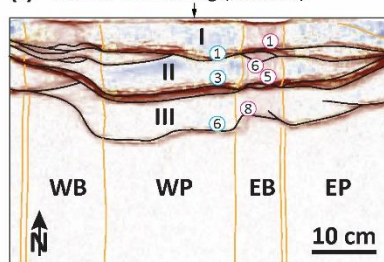
(d) 4.5 cm of shortening (10 % BS)



(e) 9 cm of shortening (20 % BS)

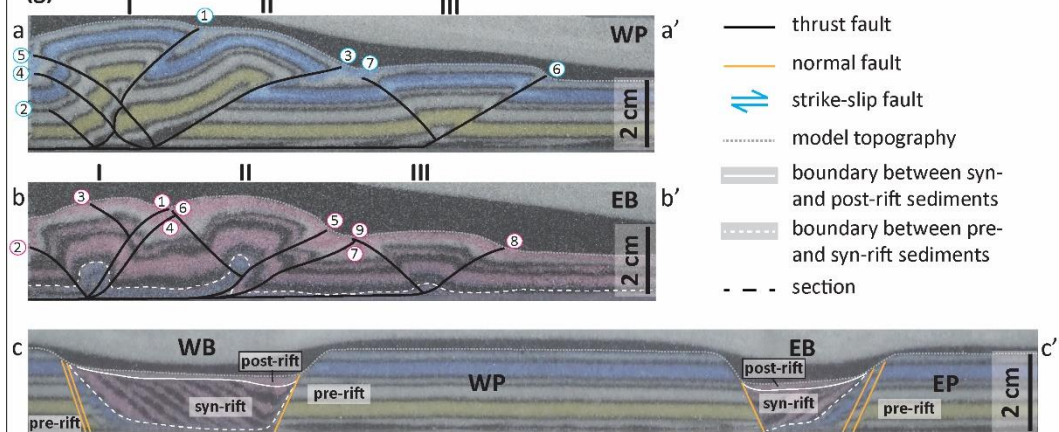


(f) 9 cm of shortening (20 % BS)



I-III thrust systems
① thrust on platform
② thrust in basin

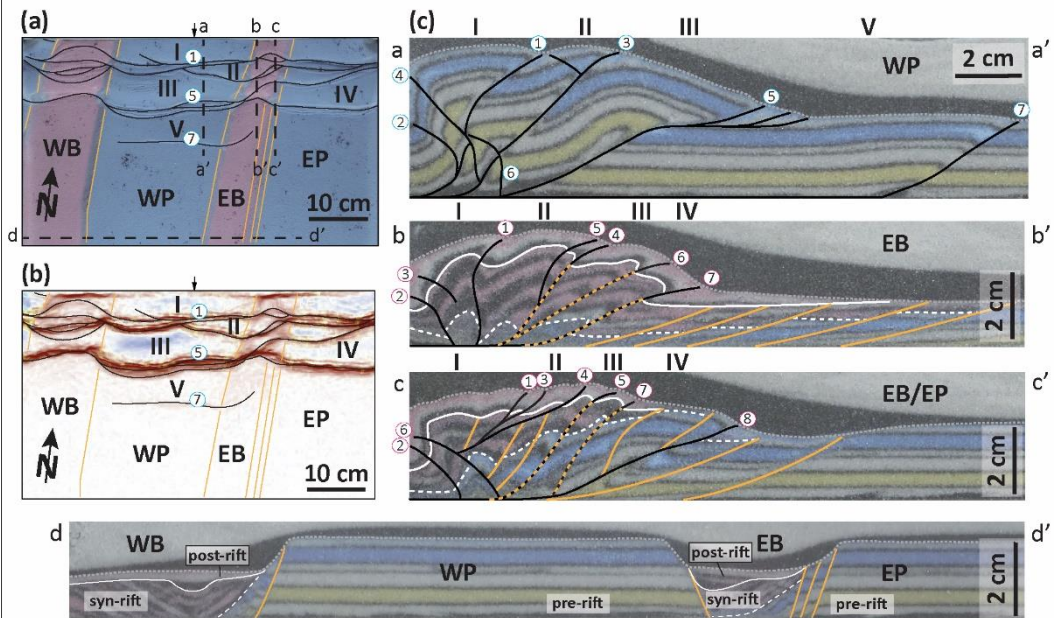
(g)



— thrust fault
— normal fault
— strike-slip fault
..... model topography
— boundary between syn- and post-rift sediments
- - - boundary between pre- and syn-rift sediments
- - - section

1285 **Figure 5. Model 1 – reference model, parallel basin inversion, quartz sand only. (a)** Interpreted top-view picture after the first phase
of extension and before shortening (0 % of bulk shortening). **(b)** Interpreted top-view picture after 2.25 cm of shortening (5 % of
bulk shortening). **(c)** Interpreted top-view picture after 4.5 cm of shortening (10 % of bulk shortening). **(d)** Map of cumulative strain
type after 4.5 cm of shortening (10 % of bulk shortening). **(e)** Interpreted top-view picture after 9 cm of shortening (20 % of bulk
shortening), **(f)** Map of cumulative strain type after 9 cm of shortening (20 % of bulk shortening). Visually interpreted structures of
1290 Fig. 5c, e overlay strain type plots in Fig. 5d, f. Strain colour legend corresponds to Fig. 5d, f. The transparency of areas with a strain
magnitude below the 90 percentile is increased for supressing areas without significant deformation. **(g)** Cross-sections of the
reference model at the end of the experiment. Grey dashed line marks the model topography at the end of the experiment. Black
and grey layers above the topography line marks the post-kinematic sand cover. Cross-section locations are shown in Fig. 5e.

Model 2



Model 3

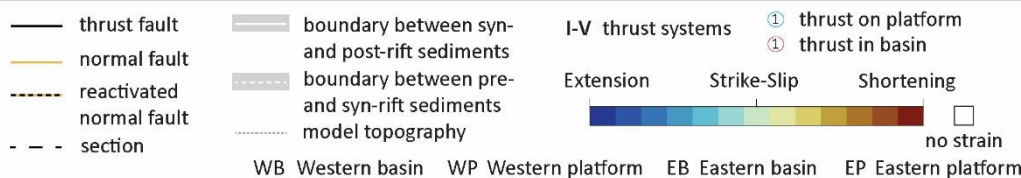
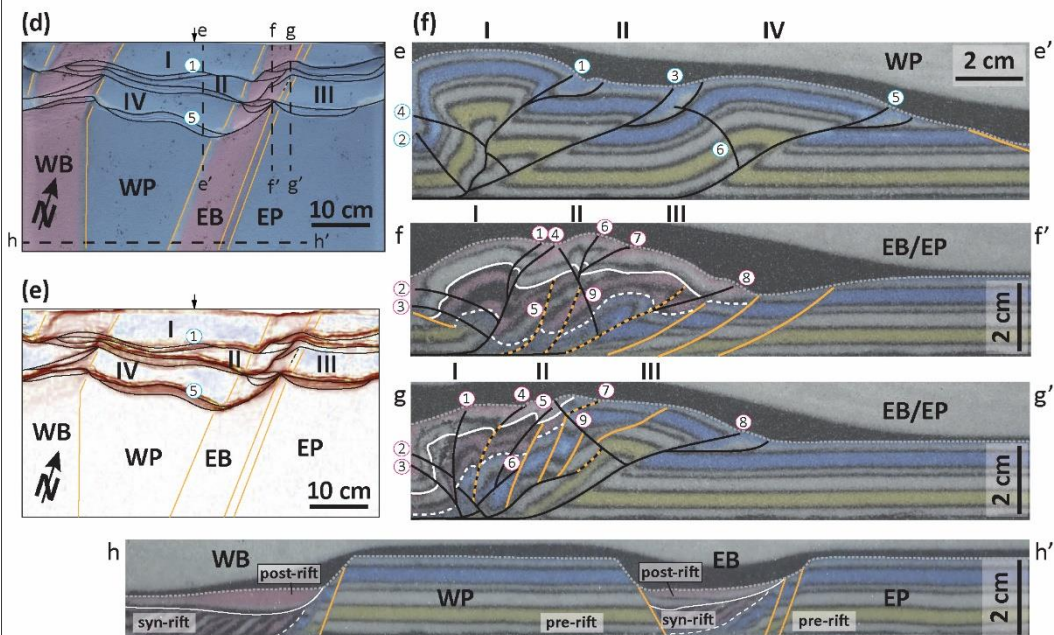
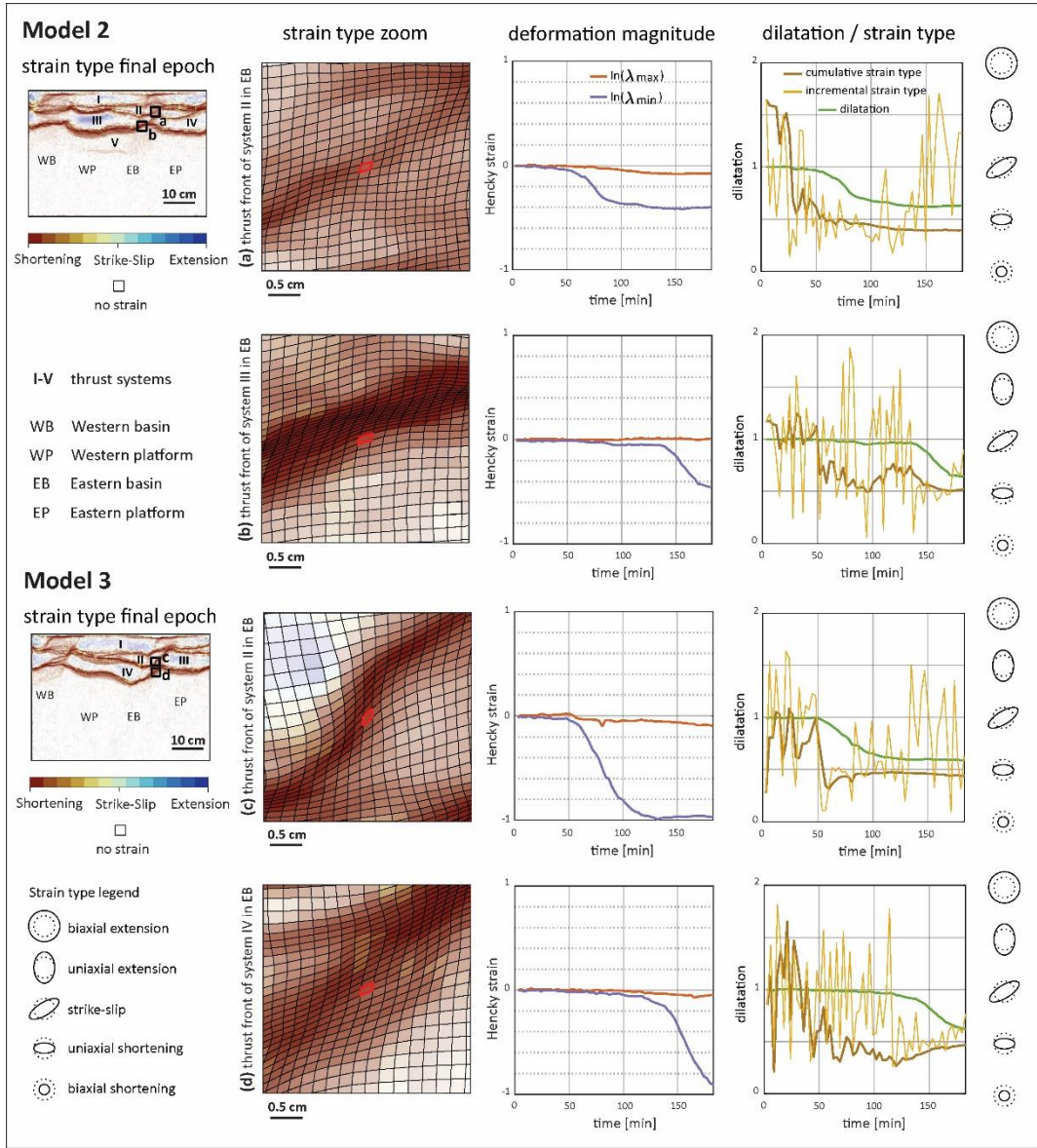


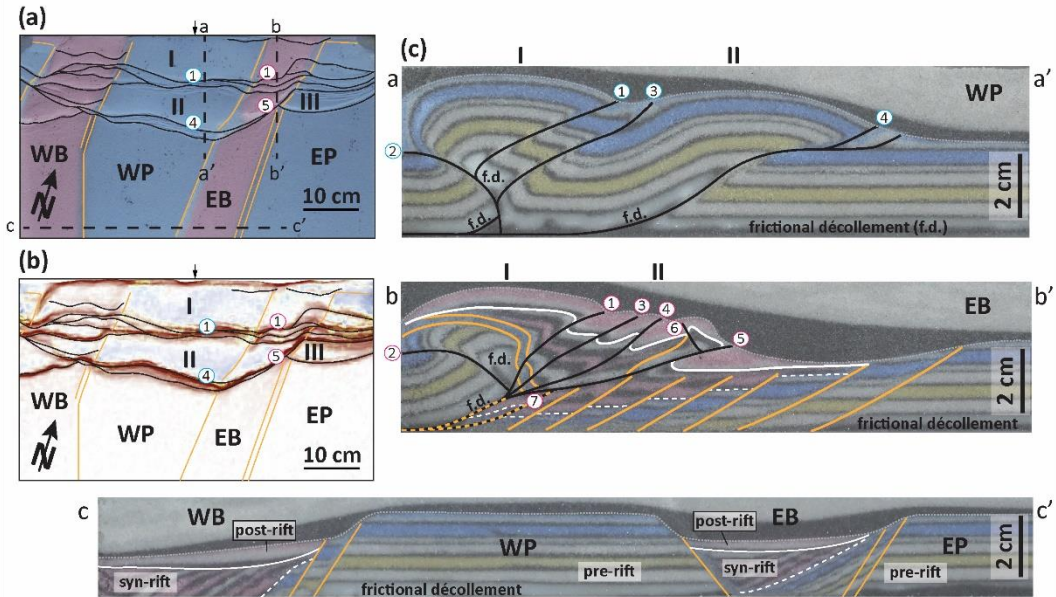
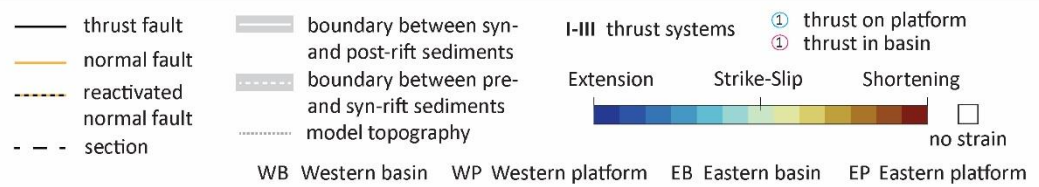
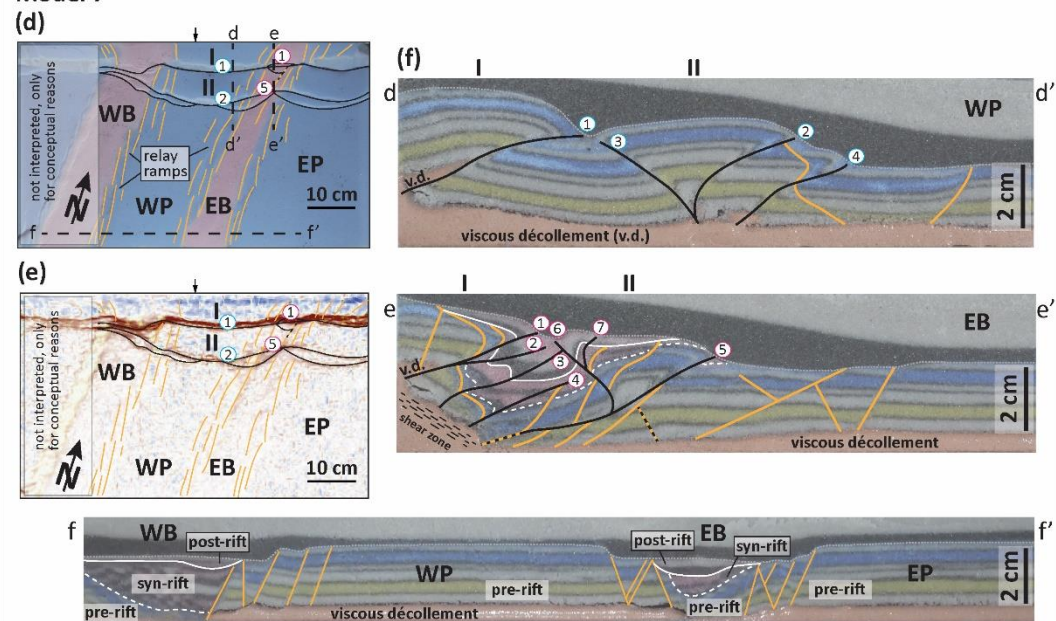
Figure 6. Model 2 and model 3 – oblique (10° , 20° , respectively) basin inversion; quartz sand only. (a) Interpreted top-view picture of model 2 after 9 cm of shortening (20 % of bulk shortening). (b) Map of cumulative strain type of model 2 after 9 cm of shortening (20 % of bulk shortening). (c) Cross-sections of model 2 at the end of the experiment. Grey dashed line marks the model topography at the end of the experiment. Black and grey layers above the topography line marks the post-kinematic sand cover. Cross-section locations are shown in Fig. 6a. Note that cross-sections a-a', b-b' and c-c' are oriented oblique (10°) to the main structures. (d) Interpreted top-view picture of model 3 after 9 cm of shortening (20 % of bulk shortening). (e) Map of cumulative strain type of model 3 after 9 cm of shortening (20 % of bulk shortening). Visually interpreted structures of Fig. 6a, d overlay strain type plots in Fig. 6b, e. Strain colour legend corresponds to Fig. Fig. 6b, e. The transparency of areas with a strain magnitude below the 90 percentile is increased for supressing areas without significant deformation. (f) Cross-sections of model 3 at the end of the experiment. Grey dashed line marks the model topography at the end of the experiment. Black and grey layers above the topography line marks the post-kinematic sand cover. Cross-section locations are shown in Fig. 6d. Note that cross-sections e-e', f-f' and g-g' are oriented oblique (20°) to the main structures.



1305

1310

Figure 7. Temporal evolution of principal stretches and strain type during the shortening phase of model 2 (a) at the thrust front of thrust system II in the eastern basin and (b) at the thrust front of thrust system III within the eastern basin and of model 3 (c) at the thrust front of thrust system II in the eastern basin and (d) at the thrust front of thrust system IV within the eastern basin. Upper left-hand panel: strain type (final) and overview of the selected areas (a) and (b) of model 2. Middle left-hand panel: strain type (final) and overview of the selected areas (c) and (d) of model 3. Left column: zoom on the strain type including the selected grid cell (outlined in red) and neighbouring grid cells (outlined in black). Middle column: temporal evolution of the logarithm of the two principal stretches (Henky strain, blue and red line). Right column: temporal evolution of dilatation, cumulative strain type, and incremental strain type.

Model 5**Model 7**

1315 **Figure 8. Model 5 and model 7 – oblique (20°) basin inversion; variation in material for basal décollement (glass beads and silicon
1320 putty, respectively). (a) Interpreted top-view picture of model 5 after 9 cm of shortening (10 % of bulk shortening). (b) Map of
1325 cumulative strain type of model 5 after 9 cm of shortening (10 % of bulk shortening). (c) Cross-sections of model 5 at the end of the
experiment. Grey dashed line marks the model topography at the end of the experiment. Black and grey layers above the topography
line mark the post-kinematic sand cover. Cross-section locations are shown in Fig. 8a. Note that the cross-sections a-a' and b-b' are
oriented oblique (20°) to the main shortening structures. (d) Interpreted top-view picture of model 7 after 9 cm of shortening (10 %
of bulk shortening). (e) Map of cumulative strain type of model 7 after 9 cm of shortening (10 % of bulk shortening). Visually
interpreted structures of Fig. 8a, d overlay strain type plots in Fig. 8b, e. Strain colour legend corresponds to Fig. 8b, e. The
transparency of areas with a strain magnitude below the 90 percentile is increased for supressing areas without significant
deformation. (f) Cross-sections of model 7 at the end of the experiment. Grey dashed line marks the model topography at the end of
the experiment. Black and grey layers above the topography line mark the post-kinematic sand cover. Cross-section locations are
shown in Fig. 8d. Note that the cross-sections d-d' and e-e' are oriented oblique (20°) to the main shortening structures.**

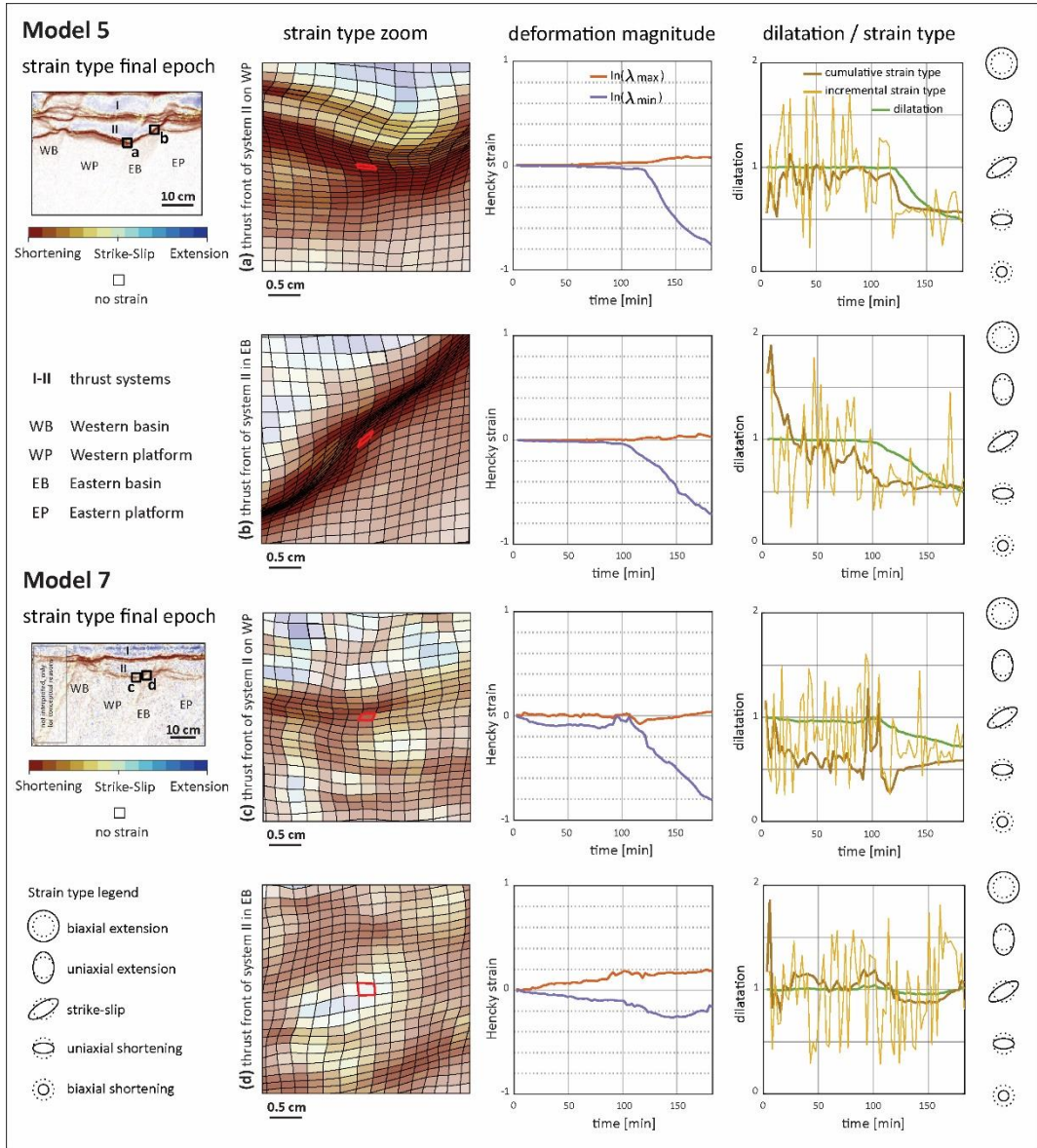


Figure 9. Temporal evolution of principal stretches and strain type during the compressional phase of model 5 (a) at the thrust front of thrust system II on the western platform and (b) at the thrust front of thrust system II within the eastern basin and of model 7 (c) at the thrust front of thrust system II on the western platform and (d) at the thrust front of thrust system II within the eastern basin. Upper left-hand panel: strain type (final) and overview of the selected areas (a) and (b) of model 5. Middle left-hand panel: strain type (final) and overview of the selected areas (c) and (d) of model 7. Left column: zoom on the strain type including the selected grid cell (outlined in red) and neighbouring grid cells (outlined in black). Middle column: temporal evolution of the logarithm of the two principal stretches (Henky strain, blue and red line). Right column: temporal evolution of dilatation, cumulative strain type, and incremental strain type.

1330

1335

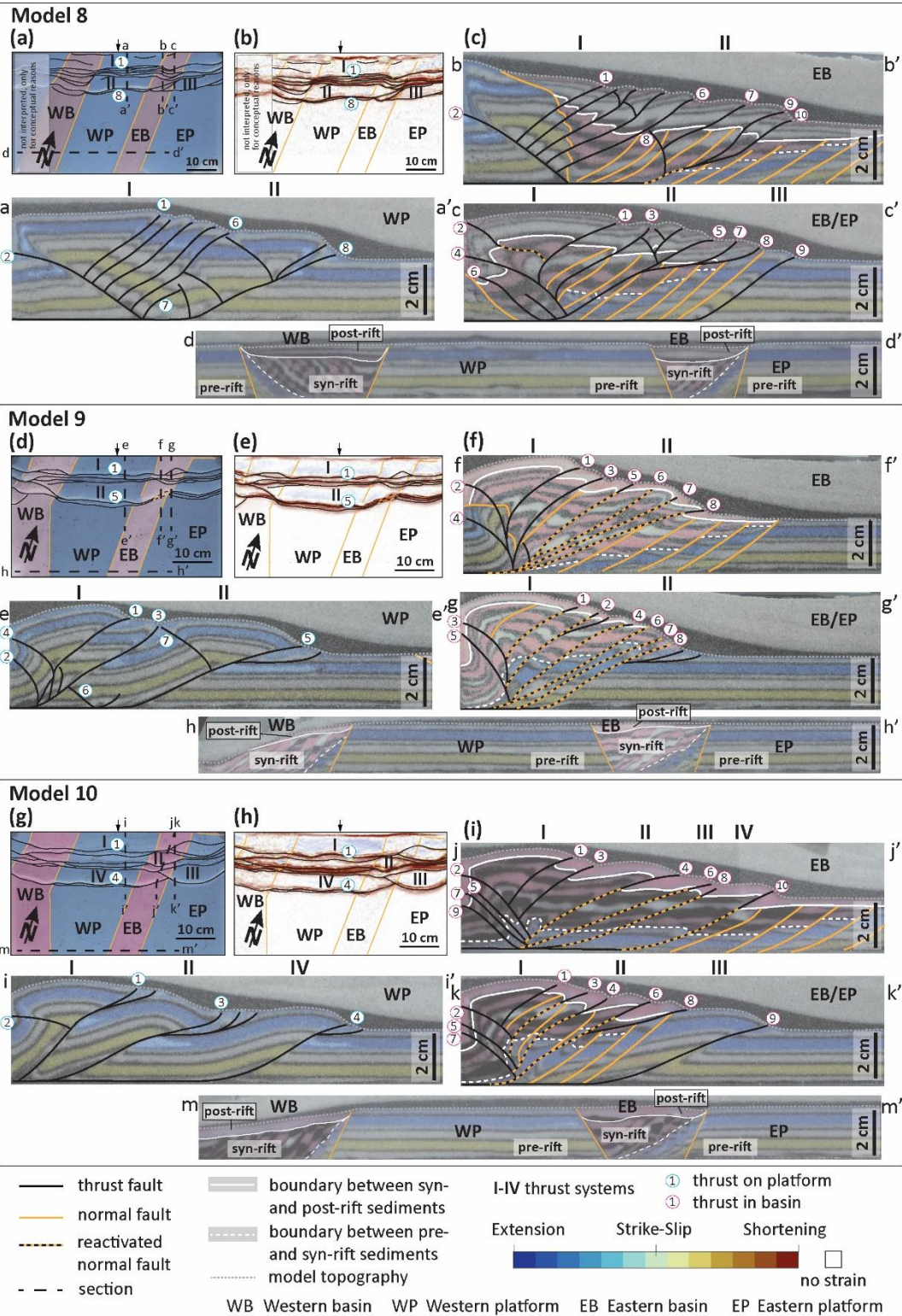


Figure 10. Model 8, model 9 and model 10 – oblique (20°) basin inversion; variation in material of the basin fill (quartz sand, feldspar sand, and glass beads, respectively). (a) Interpreted top-view picture of model 8 after 9 cm of shortening (20 % of bulk shortening). (b) Map of cumulative strain type of model 8 after 9 cm of shortening (20 % of bulk shortening). (c) Cross-sections of model 8 at the end of the experiment. Grey dashed line marks the model topography at the end of the experiment. Black and grey layers above the topography line mark the post-kinematic sand cover. Cross-section locations are shown in Fig. 10a. Note that the cross-sections a', b-b', and c-c' are oriented oblique (20°) to the main shortening structures. (d) Interpreted top-view picture of model 9 after 9 cm of shortening (20 % of bulk shortening). (e) Map of cumulative strain type of model 9 after 9 cm of shortening (20 % of bulk shortening). (f) Cross-sections of model 9 at the end of the experiment. Grey dashed line marks the model topography at the end of the experiment. Black and grey layers above the topography line mark the post-kinematic sand cover. Cross-section locations are shown in Fig. 10d. Note that the cross-sections e-e', f-f', and g-g' are oriented oblique (20°) to the main shortening structures. (g) Interpreted top-view picture of model 10 after 9 cm of shortening (20 % of bulk shortening). (h) Map of cumulative strain type of model 10 after 9 cm of shortening (20 % of bulk shortening). Visually interpreted structures of Fig. 10a, d, g overlay strain type plots in Fig. 10b, e, h. Strain colour legend corresponds to Fig. 10b, e, h. The transparency of areas with a strain magnitude below the 90 percentile is increased for supressing areas without significant deformation. (i) Cross-sections of model 10 at the end of the experiment. Grey dashed line marks the model topography at the end of the experiment. Black and grey layers above the topography line mark the post-kinematic sand cover. Cross-section locations are shown in Fig. 10g. Note that the cross-sections i-i' and k-k' are oriented oblique (20°) to the main shortening structures.

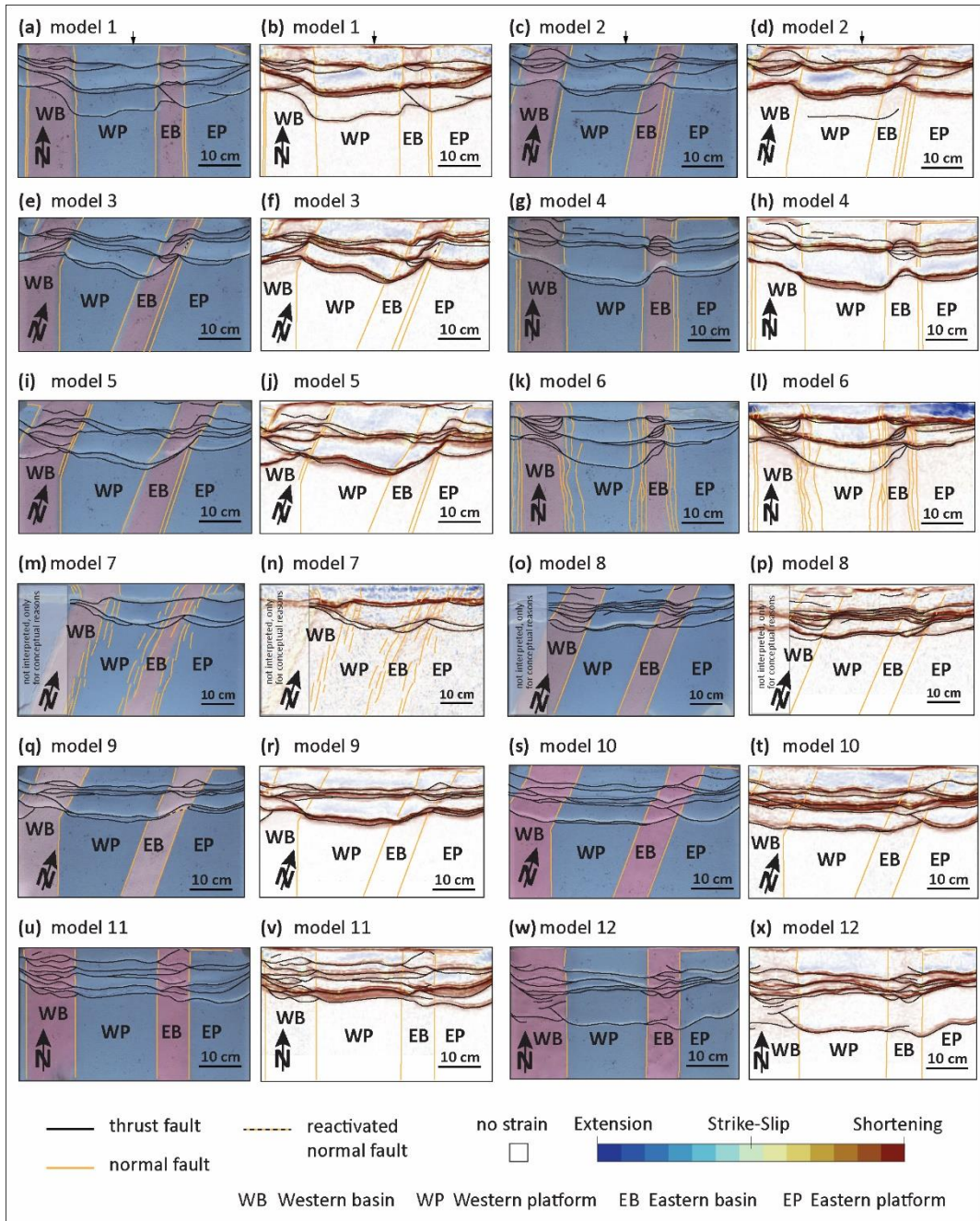


Figure 11. Interpreted top-view pictures and cumulative strain type maps of the final stages of all 12 experiments after 9 cm of shortening (20 % of bulk shortening). Visually interpreted structures of Fig. 11a, c, e, g, i, k, m, o, q, s, u, w overlay strain type plots in Fig. 11b, d, f, h, j, l, n, p, r, t, v, x. Strain colour legend corresponds to Fig. 11b, d, f, h, j, l, n, p, r, t, v, x. The transparency of areas with a strain magnitude below the 90 percentile is increased for suppressing areas without significant deformation. The black arrow in the uppermost row of panels indicates the direction of the shortening direction (i.e., moving wall) for all 12 experiments.

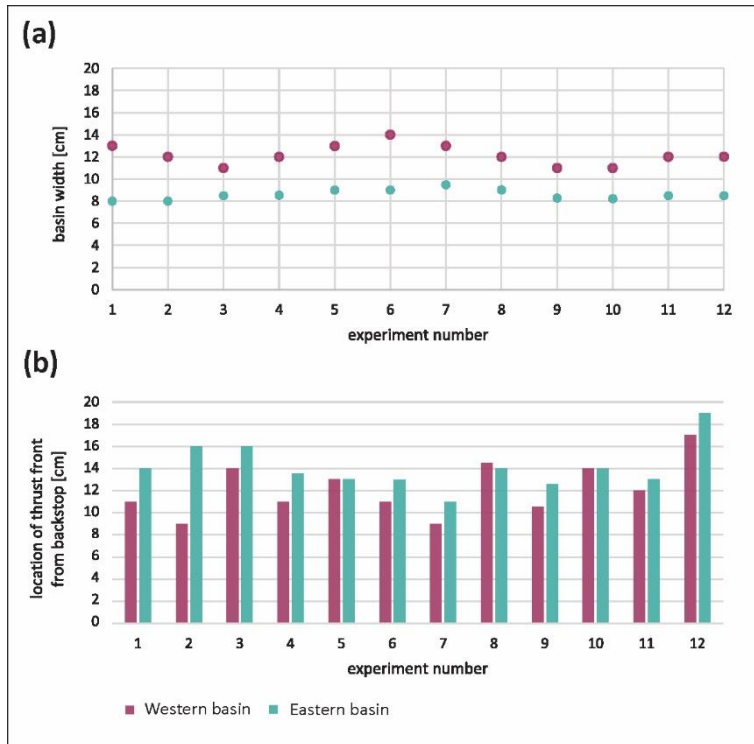


Figure 12. (a) Chart of basin widths of the western and eastern basins of each experiment, measured at the final stage (20 % of bulk shortening) of the experiment in W-E direction, perpendicular to platform boundaries. (b) Histogram showing the distance of the thrust fronts in basinal areas from the backstop, measured at the final stage (20 % of bulk shortening) of the experiment on top-view photographs.

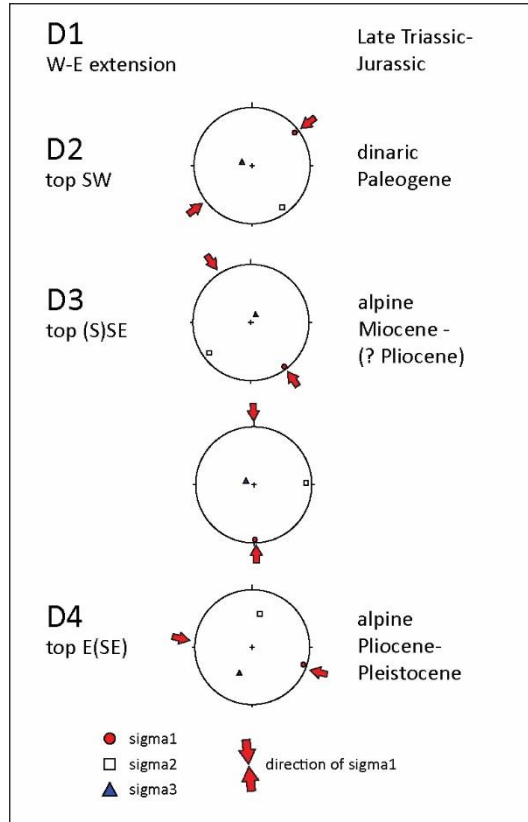
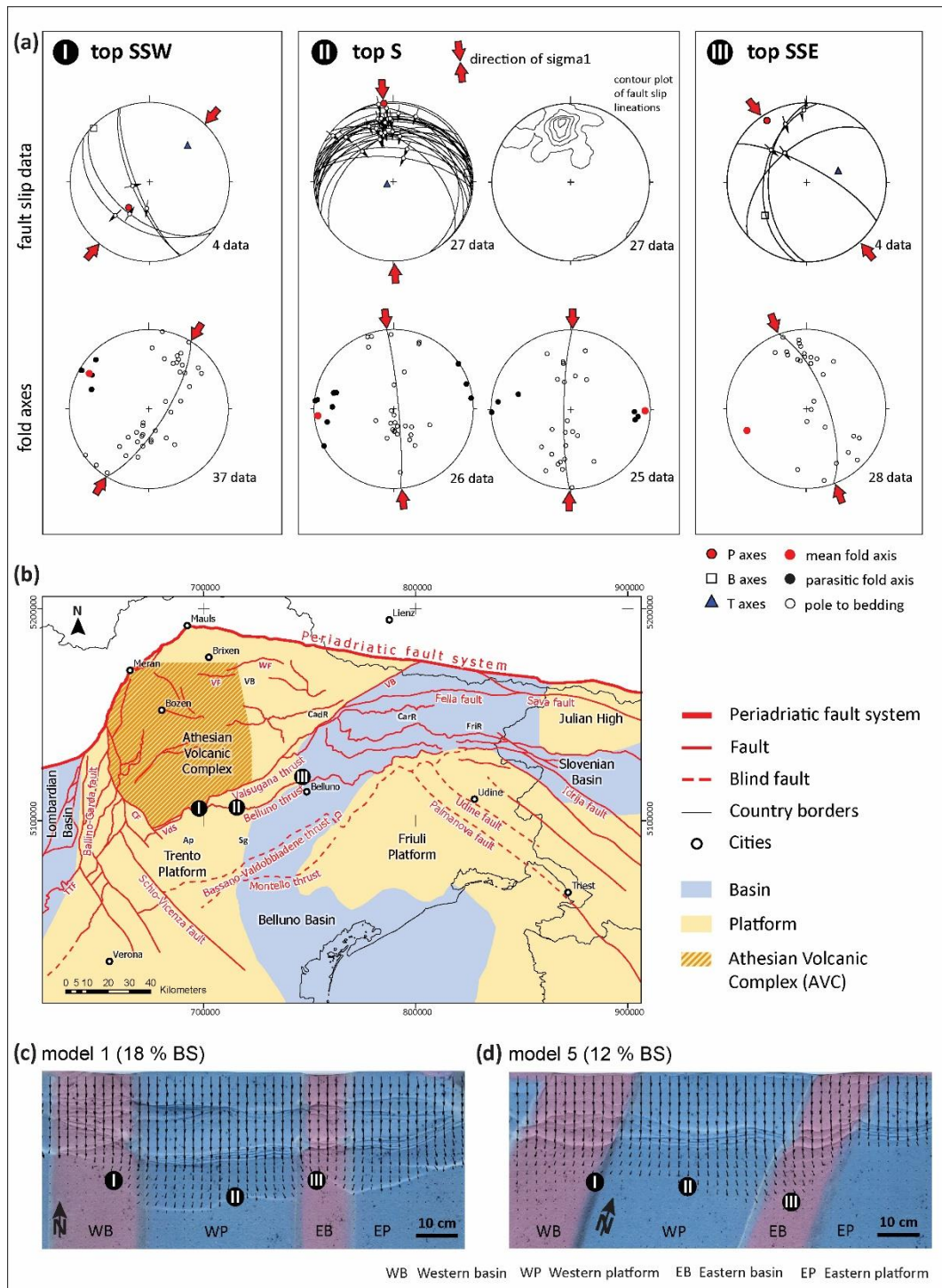


Figure 13. Schematic overview of the main deformational phases D1 to D4 of the eastern Southern Alps (compiled from Caputo (1996); Castellarin and Cantelli (2000); Caputo et al. (2010) and this study).



1370 **Figure 14.** (a) Fault slip data with local stress directions and fold axes with indicated shortening directions of the Belluno thrust
(Valsugana fault system). Locations I to III are indicated in Fig. 12b. (b) Late Triassic/Jurassic platform-basin configuration
(modified from Winterer and Bosellini, 1981; Busetti et al., 2010; Masetti et al., 2012; Martinelli et al., 2017; Picotti and Cobianchi,
2017; Picotti et al., 2022) projected over the present day geography and overlain by the tectonic map of the Dolomites Indenter
1375 (modified from Schönborn, 1999; Castellarin and Cantelli, 2000; Schmid et al., 2004; Ponton, 2010; Viscolani et al., 2020). Note the
change in shortening directions along strike of the Belluno thrust. Locations I to III represent segments of different strike of the
Belluno thrust. Coordinates are in WGS 84/UTM zones 32T and 33T. Abbreviation red: VF – Villnöss/Funes fault, WF –
Würzjoch/Passo delle Erbe fault, TTF – Tremosine-Tignale fault, VB – Val Bordaglia fault, CF – Calisio fault, VdS – Val di Sella
back-thrust, CL – Caneva line. Abbreviation black: CadR – Cadore region, CarR – Carnia region, FriR – Friuli region, VB – Val
1380 Badia/Gadertal, Ap – Asiago pop-up structure, Sg – Seren graben. (c) PIV analysed top-view picture of parallel basin inversion of
model 1 at 18 % of bulk shortening (BS). Black arrows indicate vectors of particle flow direction. (d) PIV analysed top-view picture of
oblique (20°) basin inversion of model 5 at 12 % of bulk shortening (BS). Black arrows indicate vectors of particle flow direction.

Table 1. Geometrical model parameters used in this study. Rheology of basal décollement: B – brittle, D – ductile. Material of basal décollement: qs – quartz sand, gb – glass beads, sp – silicon putty. Material of basin fill: qs – quartz sand, fs – feldspar sand, gb – glass beads.

Model number	Angle of obliquity for inversion [°]	Rheology/Material of basal décollement	Material of basin fill	Thickness brittle layer platform [cm]	Thickness brittle layer basin [cm]	Thickness ductile layer [cm]	Engine velocity extension [cm/h]	Engine velocity compression [cm/h]	Total shortening [cm]
Set 1 - Obliquity of inversion									
1	0	B/qs	qs	2.0	1.4	-	5.0	3.0	9.0
2	10	B/qs	qs	2.0	1.4	-	5.0	3.0	9.0
3	20	B/qs	qs	2.0	1.4	-	5.0	3.0	9.0
Set 2 - Rheology of décollement									
4	0	B/gb	qs	2.6	2.0	-	5.0	3.0	9.0
5	20	B/gb	qs	2.6	2.0	-	5.0	3.0	9.0
6	0	D/sp	qs	2.0	1.4	0.6	2.5	2.5	9.0
7	20	D/sp	qs	2.0	1.4	0.6	2.5	2.5	9.0
Set 3 - Rheology of basin fill									
8	20	B/qs	qs	2.0	2.0	-	5.0	3.0	9.0
9	20	B/qs	fs	2.0	2.0	-	5.0	3.0	9.0
10	20	B/qs	gb	2.0	2.0	-	5.0	3.0	9.0
11	0	B/qs	gb	2.0	2.0	-	5.0	3.0	9.0
12	0	B/gb	gb	2.6	2.6	-	5.0	3.0	9.0

Table 2. Properties for brittle and ductile material used in this study.

Material	Grain size [μm]	Density ρ [kg/m ³]	Cohesion C [Pa]	Coefficient of peak friction μ_p	Coefficient of dynamic friction μ_d	Coefficient of reactivation friction μ_r	Viscosity η [Pas]	Stress component n
Brittle								
Quartz sand	100-300	1500	10-40	0.63	0.48	0.52	-	-
Feldspar sand	100-250	1300	15-35	0.68	0.55	0.61	-	-
Glass beads	100-200	1530	25	0.48	0.40	0.44	-	-
Ductile								
PDMS + Rhodorsil gomme mixture	-	1500	-	-	-	-	3.8×10^4	1.15